Design and Evaluation of a Concentrating Solar Power System with Thermochemical Water Splitting Process for the Co-production of Hydrogen and Electricity

by

Vishnu Kumar Budama

A Dissertation Presented in Partial Fulfillment
of the Requirements for the Degree
Doctor of Philosophy

Approved March 2018 by the
Graduate Supervisory Committee:

Nathan Johnson, Chair
Ellen Stechel
Konrad Rykaczewski
Patrick Phelan
Robert Wang

ARIZONA STATE UNIVERSITY

May 2018

ABSTRACT

Thermodynamic development and balance of plant study is completed for a 30 MW solar thermochemical water splitting process that generates hydrogen gas and electric power. The generalized thermodynamic model includes 23 components and 45 states. Quasi-steady state simulations are completed for design point system sizing, annual performance analysis and sensitivity analysis. Detailed consideration is given to water splitting reaction kinetics with governing equations generalized for use with any redox-active metal oxide material. Specific results for Ceria illustrate particle reduction in two solar receivers for target oxygen partial pressure of 10 Pa and particle temperature of 1773 K at a design point DNI of 900 W/m^2. Sizes of the recuperator, steam generator and hydrogen separator are calculated at the design point DNI to achieve 100,000 kg of hydrogen production per day from the plant. The total system efficiency of 39.52% is comprised of 50.7% hydrogen fraction and 19.62% electrical fraction. Total plant capital costs and operating costs are estimated to equate a hydrogen production cost of $4.40 per kg for a 25-year plant life. Sensitivity analysis explores the effect of environmental parameters and design parameters on system performance and cost. Improving recuperator effectiveness from 0.7 to 0.8 is a high-value design modification resulting in a 12.1% decrease in hydrogen cost for a modest 2.0% increase in plant $2.85M. At the same time, system efficiency is relatively inelastic to recuperator effectiveness because 81% of excess heat is recovered from the system for electricity production 39 MWh/day and revenue is $0.04 per kWh. Increasing water inlet pressure up to 20 bar reduces the size and cost of super heaters but further pressure rises increasing pump at a rate that outweighs super heater cost savings.

ACKNOWLEDGMENTS

Firstly, I would like to express my sincere gratitude to my advisor, Dr. Nathan Johnson, for his tremendous support over the years. I appreciate his personal attention, care and direction during tough times. His guidance is invaluable during writing of journal papers and dissertation thesis. I could not have imagined having a better advisor for my research.

Besides my advisor, I am thankful to Dr. Ellen Stechel, who have been guiding me throughout my Ph.D. I appreciate her patience in answering my question during technical discussions. It was great working with her.

I would like to thank the rest of my thesis committee Dr. Konrad Rykaczewski, Dr. Patrick Phelan and Dr. Robert Wang for their insightful comments and encouragement. Their feedback on my research work is very precious to improve the quality of my research work.

The U.S. Department of Energy (DOE) Fuel Cell Technology Office (FCTO) provided funding for the project entitled High Performance Reduction/Oxidation Metal Oxides for Thermochemical reactor for hydrogen production under award number DE-FOA-0000826-1526. The authors would like to thank all the members of the Hydrogen team for useful conversations and insights.

Sandia National Laboratories is a multi-mission laboratory managed and operated by National Technology and Engineering Solutions of Sandia, LLC, a wholly owned subsidiary of Honeywell International, Inc., for the U.S. Department of Energy's National Nuclear Security Administration under contract DE-NA-0003525.

TABLE OF CONTENTS

LIST OF TABLES

Table Page

LIST OF FIGURES

Figure Page

Figure Page

NOMENCLATURE

Variable	Description	Units
DNI	Direct Normal Irradiance	W/m^2
$\dot{n}_p$	Molar flow rate of particles	mol/s
$\dot{m}_p$	Mass flow rate of particles	kg/s
$\dot{n}_g$	Molar flow rate of steam into water splitting reactor	mol/s
σ	Stefan-Boltzman constant	W-m^2-K^4
A_{SR1}, A_{SR2}	External surface area of SR1 and SR2	m^2
A_{ap1}, A_{ap2}	Aperture area of SR1 and SR2	m^2
A_t	Total surface area of the tubes of recuperator	m^2
h_{loss}	Convection heat transfer coefficient	W/m^2-K
$\dot{C}_r$	Heat capacity of particles in recuperator	J/K-s
ε_r	Effectiveness of the recuperator	-
ε_o	Effectiveness of re-oxidation reaction	-
α	Excess steam factor	-
Q_{lat}	Latent heat of water	J/mol
$\dot{Q}_{ext}$	Exotherm heat release during re-oxidation reaction	J/s
T_{sat}	Saturation temperature of water	K
h_{elv}	Elevator height	m
$P_{r,vp1}, P_{r,vp2}$	Pressure ratio in vacuum pump 1 and 2	-
$P_{r,sp}$	Pressure ratio in steam pump	-
$P_{r,hp}$	Pressure ratio in hydrogen pump	-
η_{vp1}, η_{vp2}	Efficiency of vacuum pump 1 and 2	-
η_{wp}	Efficiency of water pump	-
η_{sp}	Efficiency of steam pump	-
η_{hp}	Efficiency of hydrogen pump	-
η_{elv}	Elevator mechanical efficiency	-
η_R	Heat to mechanical conversion (Rankine cycle) efficiency	-
η_{gen}	Mechanical to electrical conversion efficiency	-
η_{etm}	Electrical to mechanical conversion efficiency	-
HHV	Higher heating value of Hydrogen	J/mol
$\dot{V}_w$	Volumetric flow rate of water	m^3/s

M_w	Molecular weight of water	kg/mol
ρ_w	Density of water	kg/m^3
H_{loss}	Total head loss in water loop	m
g	Acceleration due to gravity	m/s^2
R	Universal gas constant	J/mol-K
$c_{w,sat}$	Specific heat of water at saturation temperature	J/mol-K
$c_{s,sat}$	Specific heat of steam at saturation temperature	J/mol-K
T_0	Ambient air temperature	K
$c_{p,i}$	Specific heat in stream *i*	J/mol-K
T_i	Temperature of stream *i*	K
h_i	Enthalpy of stream *i*	J/mol
$\dot{n}_i$	Flow rate in stream *i*	mol/s
$\dot{E}_i$	Energy of stream *i*	J/s

CHAPTER 1

INTRODUCTION

1.1 Introduction

Growing world energy consumption and the associated rise in fossil fuel use is the leading cause of increasing carbon dioxide emissions [1], [2], [3]. Alternative low-carbon fuels such as biodiesel, methanol, ethanol, hydrogen and natural gas are needed for both for stationary and transportation applications [4]. Hydrogen is considered a prevailing option for its high energy content yielding 122 kJ/gram, which is 2.75 times greater than that of hydrocarbon fuels [5]. The absence of carbon emissions in hydrogen fuel cells is another attraction of a hydrogen-based economy fuel [2], [6]. However, certain processes for producing hydrogen, such as reforming, release carbon dioxide when hydrogen is stripped from hydrocarbon fuels [7]. The costs of such solutions are also high making hydrogen a niche solution at only 3% of the total world energy consumption [8]. Hydrogen production processes using solar, and other renewable energy, have the potential to generate hydrogen with low emissions or no emissions and through advanced technologies and system designs could have the potential to deliver low-cost hydrogen at scale [9], [10].

This study introduces a quasi-dynamic thermodynamic model for a hydrogen production plant using concentrating solar to drive a thermochemical water splitting process. Redox active metal oxide materials are first reduced in a multi-stage cascading reactor and then reoxidized through contact with steam to yield hydrogen. Ceria is used as the baseline material because of its well-known properties but other materials could be readily substituted into the generalized thermodynamic model. Detailed consideration is given to plant system configuration, component selection and sizing, excess heat recovery

and power generation, and water splitting kinetics to identify optimal operating points for hydrogen production and system efficiency within system-wide thermodynamic and practical limits. Results show how heat energy wasted in a conventional thermochemical reactor can be recuperated to generate electricity and significantly improve system efficiency and output across a wide range of operating conditions.

The second part of this work completes system sizing and cost estimation for a plant designed to produce 100,000 kg of hydrogen production per day. Component sizing is based on total energy conversion in each component and considers other design features and parameters that affect performance and cost. The study introduces a new recuperator design for particle-particle heat exchange and a steam generator to extract excess heat from particles and hydrogen separator. Ultimately the cost to produce hydrogen is estimated using the capital cost, land cost, maintenance costs and financing costs for a plant with a 25-year lifetime.

1.2. Thermochemical Water-splitting Cycle

Figure 1.1 shows a diagram depicting a two-step solar thermochemical reactor for hydrogen fuel production. Metal oxide particles undergo cycle of endothermic and exothermic reactions in two separate chambers. Thermal reduction reaction occurs as the particles are heated using concentrated solar radiation and particles release oxygen atoms during this reaction. The reduced particles enter the fuel production reactor where they re-oxidize with steam to produce hydrogen fuel. Heat is recuperated between the two steps within the cycle to improve efficiency [11]. The chemical reactions are given in Eqs. 1.1-1.4.

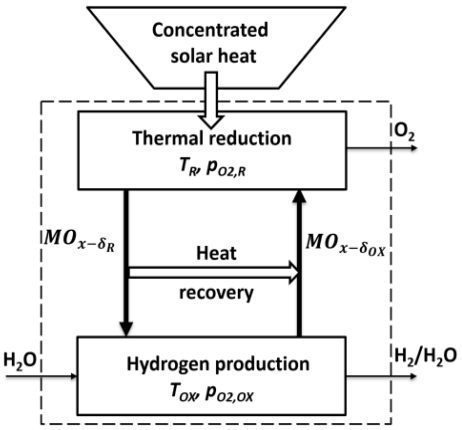

1.1. Schematic of thermochemical water-splitting cycle

Reduction: $$\frac{1}{\Delta\delta}\ MO_{x-\delta_{ox}} \rightarrow \frac{1}{\Delta\delta}\ MO_{x-\delta_R} + \frac{1}{2}O_2 \quad (1.1)$$

Re-oxidation: $$\frac{1}{\Delta\delta}\ MO_{x-\delta_R} + H_2O \rightarrow \frac{1}{\Delta\delta} MO_{x-\delta_{ox}} + H_2 \quad (1.2)$$

Net: $$H_2O \rightarrow H_2 + \frac{1}{2}O_2 \quad (1.3)$$

$$\Delta\delta = \delta_R - \delta_{ox} \quad (1.4)$$

A two-step thermochemical cycle for water-splitting using solar as primary source of energy is growing technology to produce hydrogen fuel [12], [13]. This cycle consists of one thermal reduction step at high temperature and low pressure followed by re-oxidation at lower temperature and near atmospheric pressure [14]. This separates the two chemical steps temporally or spatially and avoids to the mixing of hydrogen and oxygen which is explosive. This type of cycle was first introduced by Nakamura using oxides of Ferrite [15]. Volatile metal oxides of Zn, Cd and Ge were extensively studied for thermochemical water splitting applications [16]. One of the challenge with ZnO is it reduces all the way to gaseous metal and quenching is needed to avoid recombination [14], [17]. All volatile metal oxides need quenching to separate oxygen from metal oxide [18].

Ceria is considered for thermochemical water-splitting applications because of its fuel production kinetics and it stable high temperatures [19].

Maintaining low partial pressure of oxygen in the thermal reduction chamber is a major challenge in thermochemical cycles. Inert gas sweeping, and vacuum pumping are the two solutions to maintain low partial pressure in reduction step [20]. Inert gas sweeping requires heat recovery at high temperature and an inert gas purification plant [21]. Considering the high volumetric flows at low pressures and associated oxygen gas velocities, the resulting pumping speed increases if a single stage is the limiting factor, but Ermanoski showed that a pressure of 10 Pa can be achieved by using a pressure cascade in which multiple thermal reduction chambers successively decrease in pressure [20]. Vacuum pump efficiency is not constant at all pressures and rapidly decreases below 10 Pa [21].

CHAPTER 2

Thermodynamic Development and Design of a Concentrating Solar Thermochemical Water-Splitting Process for Co-production of Hydrogen and Electricity

In preparation for submission to *Hydrogen Energy* journal

Abstract–A concentrating solar plant is proposed for a thermochemical water-splitting with excess heat used for electricity generation in an organic Rankine cycle. The quasi-steady state thermodynamic model consisting of 23 components and 45 states uses adjustable design parameters to optimize hydrogen production and system efficiency. The plant design and associated thermodynamic model demonstrate that cerium oxide is suitable for thermochemical water-splitting cycles involving the co-production of hydrogen and electricity. Design point analyses at 900 W/m^2 DNI indicate that a single tower with solar radiation input of 27.74 MW and an aperture area of 9.424 m^2 yields 10.96 MW total output comprised of 5.55 MW hydrogen (Gibbs free energy) and 5.41 MW net electricity after subtracting off 21.96% of total power generation for auxiliary loads. Pure hydrogen output is 20.73 GWh/year (HHV) and 17.20 GWh/year (Gibbs free energy) or an annual average of 522 tonne/year with net electricity generation at 14.52 GWh/year using TMY3 data from Daggett, California, USA. Annual average efficiency is 38.14% with the consistent hydrogen factor and electrical factor being 54.3% and 45.7%, respectively. Sensitivity analyses illustrate that increases in particle loop recuperator effectiveness create an increase in hydrogen production and a decrease in electricity generation. Further, recuperator effectiveness has a measurable effect on hydrogen

production, but has limited impact on total system efficiency given that 80.85% of excess heat is recuperated within the system for electricity generation.

2.1. Introduction

Fossil fuels account for 87% of world-wide primary energy use, with leading contributors including electricity generation, transportation, space heating, and process heat [1]–[4]. The reliance on fossil fuels is expected to decrease over the next several decades as the global energy market is decarbonized [5]–[7]. Increasing amounts of solar and wind technologies are being installed for electricity generation, and while the adoption of electrical vehicles has grown, gaseous and liquid fossil-based hydrocarbons will be hard to displace given they are energy dense, easy to transport, generally low-cost, and supported by a vast system of physical infrastructure and commercial institutions [7]–[13]. This future suggests significant commercial potential in creating renewable-based hydrogen and hydrocarbon fuels as an alternative to traditional hydrocarbon fossil fuels for a range of stationary and mobile applications.

Pathways to produce pure hydrogen include electrolysis, thermolysis, photo-electro- chemistry, thermochemical, coal gasification, and natural gas reforming [11], [14]–[23]. Thermolysis breaks down molecules into constituent parts but requires high temperatures reaching 2500 K [24]. More established approaches include coal gasification and natural gas reforming but create CO_2 emissions when extracting hydrogen from a C_xH_y resource [25]. A promising alternative is to use concentrating solar for heat input into a thermochemical reaction with redox-active metal oxide particles to split water and yield hydrogen [25]–[33]. The produced hydrogen can be used directly for internal combustion and motive work, in a fuel cell for electricity generation, as a reductant in metallurgical

applications, and can be combined with renewable carbon resources to synthesize a sustainable hydrocarbon fuel that directly replaces fossil fuels in transportation, stationary power, and heating.

This study advances solar thermochemical water-splitting research with a detailed thermodynamic model of the full production plant and co-production added to create electricity, in addition to hydrogen, to improve system efficiency. The redox-active metal oxide material is first reduced in a multi-stage cascading reactor and then re-oxidized through direct contact with steam to yield hydrogen [34], [35]. Ceria is used as the reference material because of its well-known properties but other materials could be readily substituted into the generalized thermodynamic model. Detailed consideration is given to plant system configuration, component selection and sizing, and excess heat recovery and power generation. Potential limitations of water-splitting kinetics are also expressed. Sensitivity analysis is used to evaluate the impact of design parameters and state points to improve hydrogen productivity and system efficiency. Results show how waste heat can be recuperated to generate electricity and significantly improve system efficiency and overall productivity across a range of operating conditions

2.2. Thermochemical Water-splitting Cycle

A thermochemical water-splitting process using redox-active metal oxides consists of two steps: (i) endothermic reduction at high temperature and low oxygen partial pressure, and (ii) exothermic re-oxidation with steam reactant to yield hydrogen [26], [36]–[38]. This thermochemical cycle was first developed by Nakamura in 1977 using the stoichiometric metal oxide $Fe_3O_4/3FeO$ with further studies being completed for volatile

oxides of Zn, Cd, and Ge [17], [39]–[41]. ZnO decomposes at 2300 K, above its melting point, limiting the feasibility of ZnO for water-splitting because the separation of Zn and O_2 requires either quenching or an electrolytic process [42], [43]. The decomposition of CdO was experimentally demonstrated between the temperatures 1423-1723 K but quenching is also required to separate Cd and O_2 [17]. More recent research into ceria, CeO_2, has shown broader application due to rapid fuel production kinetics albeit limited off-stoichiometry [44]–[50]. Perovskites also contain a promising class of redox-active metal oxides for water-splitting applications [51], [52].

The generalized reduction and re-oxidation reactions given in Eq. 1 and Eq. 2, respectively, yield oxygen and hydrogen gas as the net products described in Eq. 3 [30], [53]. This cycle is shown graphically in Fig. 1. The endothermic reduction reaction of the metal oxide, MO, occurs at temperatures above 1573 K and oxygen partial pressures below 1000 Pa. The exothermic re-oxidation reaction occurs when the metal oxide interacts with steam at temperatures below 1473 K and near atmospheric pressure [29]. A mixture of hydrogen and steam exits the water-splitting reactor with sufficient excess steam to permit the forward reaction to overcome the back reaction. The reduced metal oxide generally cools between the two steps and the amount of cooling decreases with increase in extent of reduction per unit of hydrogen produced. Hydrogen production is proportional to the difference in the extent of reduction between the reduction and re-oxidation reactions as expressed in Eq. 4. Assuming no kinetic limitations, the extent of thermal reduction is determined by material properties, reduction temperature, and the oxygen partial pressure in the solar stage-reduction reactor. The redox-active material is assumed to be in particle form. Heat is recovered from the hot particles to achieve higher cycle efficiencies.

$$\frac{1}{\Delta\delta}\, MO_{x-\delta_{OX}} \rightarrow \frac{1}{\Delta\delta}\, MO_{x-\delta_R} + \frac{1}{2} O_2 \quad (1)$$

$$\frac{1}{\Delta\delta}\, MO_{x-\delta_R} + H_2O \rightarrow \frac{1}{\Delta\delta} MO_{x-\delta_{OX}} + H_2 \quad (2)$$

$$H_2O \rightarrow H_2 + \frac{1}{2} O_2 \quad (3)$$

$$\Delta\delta = \delta_R - \delta_{OX} \quad (4)$$

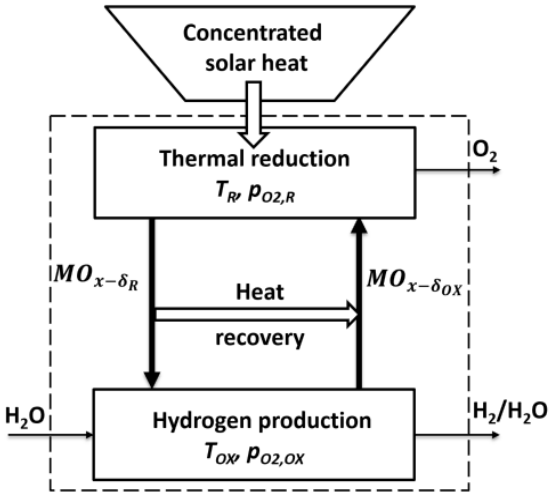

Figure 1. Simplified schematic of the two-step thermochemical cycle for water-splitting using redox-active metal oxide materials

Here $p_{O2,R}$ and $p_{O2,OX}$ are partial pressures of oxygen in reduction and re-oxidation reactors

T_R and T_{OX} are reduction and re-oxidation temperatures.

A previous study of this thermodynamic cycle calculated hydrogen conversion efficiencies between 6-30% using ceria, CeO_2, with varying oxygen partial pressure from 100,000 Pa to 1 Pa obtained using a vacuum pump at a fixed reduction temperature of 1773 K, a fixed re-oxidation temperature of 1373 K at ambient pressure, and a recuperator effectiveness of 0.5 [29], [38], [54].

2.3. Model Development

Figure 2.2 shows a component diagram of the hydrogen production system with electricity coproduction. A total of 23 components and 45 streams are represented across two sub-systems for hydrogen production and electricity production, with the associated solar field and supplemental feedwater tank outside the system boundary. This model was developed for general use with a range of redox active materials to permit extension in other studies.

The hydrogen production sub-system includes a particle loop in which particles pass through two solar receivers, a recuperator, a steam generator, a water splitting reactor, and a particle elevator. Auxiliary components to support the water splitting process include vacuum pumps, heat exchangers, a water pump, a steam pump, a hydrogen pump, a steam mixing chamber, a water tank, a preheater, a hydrogen separator, and secondary concentrators. The electricity coproduction sub-system is an organic Rankine cycle. Gas and fluid properties including specific heats, entropies, and enthalpies were taken from the Engineering Equation Solver (EES) thermo-fluid materials library as functions of temperature and pressure.

The solar field supplies radiation to increase particle temperature by direct absorption and thermally reduce to the equilibrium reduction extent at the targeted temperature and partial pressure of oxygen (achieved here by evacuating the receiver to the desired pressure). Eq. 2.5 gives the total solar flux into all receivers, $\dot{Q}_1$ is total solar flux onto the solar field of mirrors; $\dot{Q}_2$ and $\dot{Q}_3$ are the radiation supplied to solar receiver 1 and solar receiver 2, respectively; $\dot{Q}_4$ represents the heat recovered from intentional spillage and from cooling the secondary concentrators on the solar receivers, and $\dot{Q}_{36}$ is solar field

losses. Particle flow rate is determined from an energy balance around solar receiver 2 and varies with changes in solar irradiance.

$$\dot{Q}_1 = \dot{Q}_2 + \dot{Q}_3 + \dot{Q}_4 - \dot{Q}_{36} \tag{2.5}$$

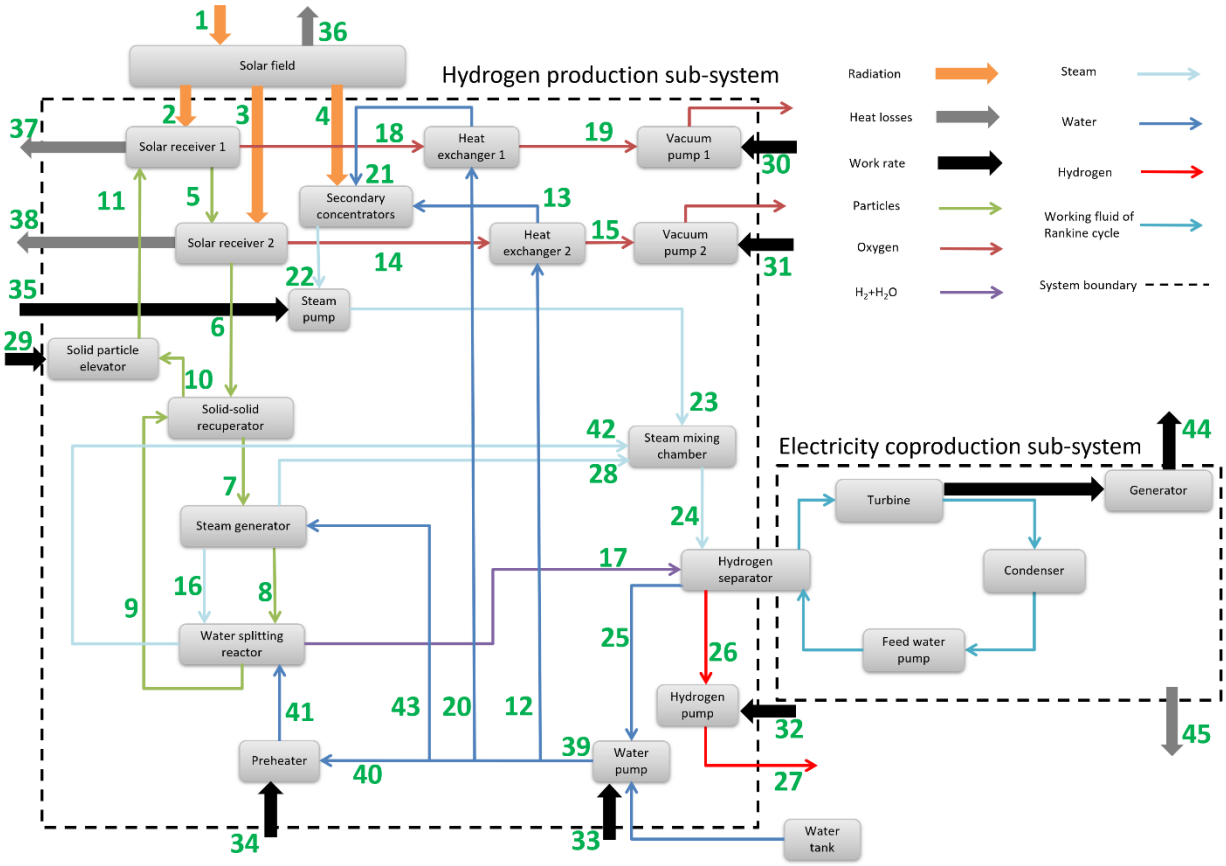

Figure 2.2. Component diagram of solar thermal system for hydrogen and electricity production

2.3.1 Hydrogen Production Sub-system

Solar receiver 1 and solar receiver 2: Two solar receivers provide the multistage cascading pressure reduction from ambient pressure to a lower oxygen partial pressure. This approach avoids using inert sweep gas and resolves limitations in achieving low pressures in a single step due to volumetric flows and pump speed [17], [20], [21]. More stages can be added to reach higher temperature and lower partial pressure requirements

that may be needed for other redox-active materials. Each stage can have one or more apertures, with three apertures for each receiver used in this study. Oxygen partial pressure is assumed constant in each receiver. Solar receiver 1 heats particles in a closed volumetric receiver with the majority of energy used for sensible energy change and minimal thermal reduction. Solar receiver 2 increases particle temperature to designed reduction temperature and reduces oxygen partial pressure to produce the target reduction extent, δ_R. Heat flux into solar receivers 1 and 2 are given in Eqs. 2.6 and 2.8, respectively, with corresponding losses from each expressed in Eqs. 2.7 and 2.9, respectively. The surface temperature for radiation and convection loss calculations is approximated using the average temperature between particle inlet and exit conditions. The overestimation of radiation losses is less than 5%. This overestimates convective losses when noting that receiver insulation will reduce the external surface temperature far less than the approximated 1700 K.

$$\dot{Q}_2 = \dot{E}_{18} + \dot{Q}_{37} + \left(\dot{n}_p \cdot (h_5 - h_{11})\right) \tag{2.6}$$

$$\dot{Q}_{37} = \left(\sigma \cdot A_{ap1} \cdot \left(\frac{T_5^4 + T_{11}^4}{2} - T_0^4\right)\right) + \left(h_{loss} \cdot A_{SR1} \cdot \left(\frac{T_5 + T_{11}}{2} - T_0\right)\right) \tag{2.7}$$

$$\dot{Q}_3 = \dot{E}_{14} + \dot{Q}_{38} + \left(\dot{n}_p \cdot (h_6 - h_5)\right) \tag{2.8}$$

$$\dot{Q}_{38} = \left(\sigma \cdot A_{ap2} \cdot \left(\frac{T_6^4 + T_5^4}{2} - T_0^4\right)\right) + \left(h_{loss} \cdot A_{SR2} \cdot \left(\frac{T_6 + T_5}{2} - T_0\right)\right) \tag{2.9}$$

Secondary concentrators: Secondary concentrators improve optical efficiency by focusing sunlight into receiver apertures. Saturated water is circulated to cool the concentrators with flow rate that varies such that the exit stream is saturated steam. The quantity of heat flux into secondary concentrators is given in Eq. 2.10.

$$\dot{Q}_4 = q_{lat} \cdot (\dot{n}_{13} + \dot{n}_{21}) \tag{2.10}$$

Solid-solid recuperator: A recuperator reduces solar input requirements and improve cycle efficiency [30] [31]. It further benefits cycle efficiency because hydrogen production increases as the temperature difference widens between reduction and re-oxidation, to an amount determined by the extent of reduction [44], and avoids the need for a heat rejecter in the particle loop.

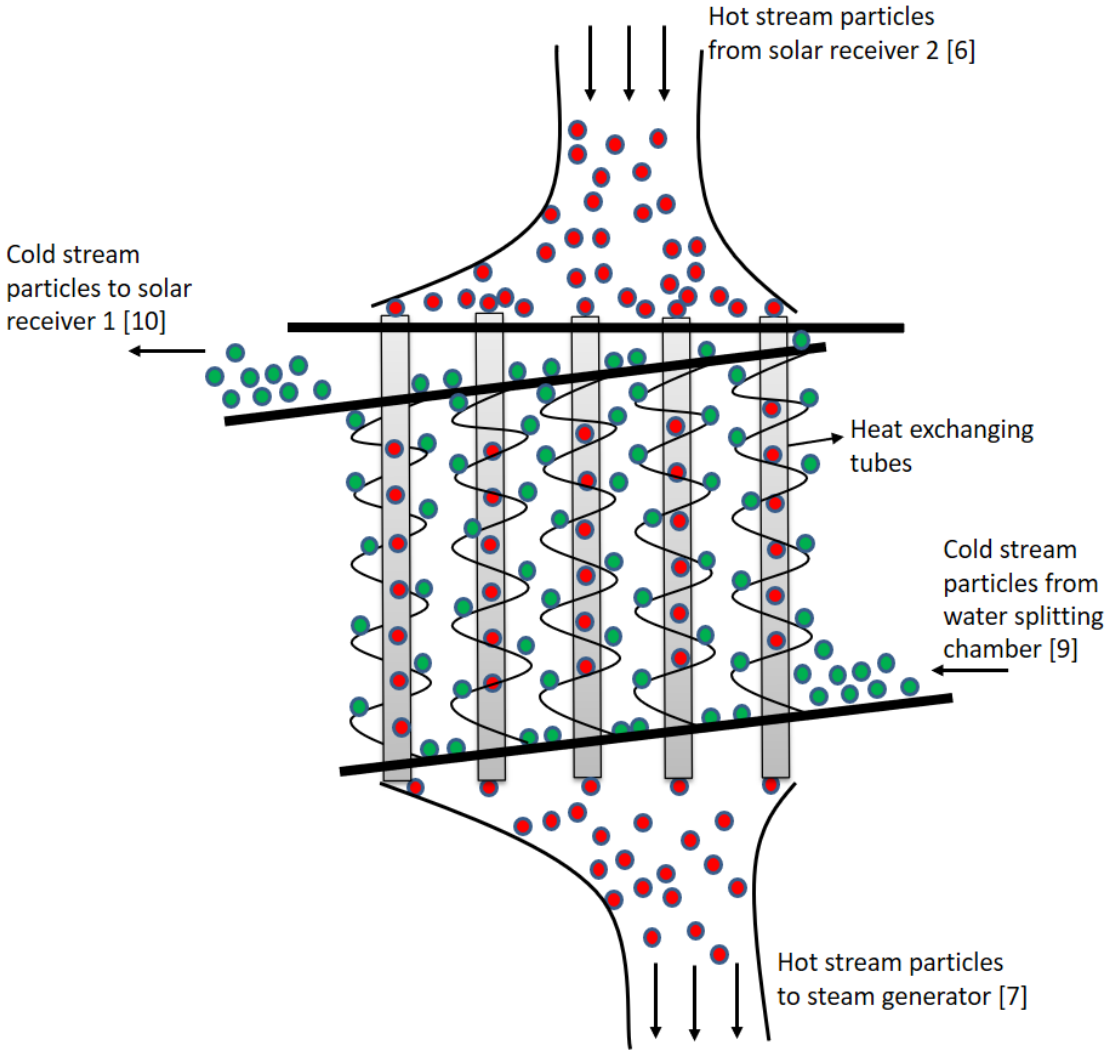

Figure 2.3. Solid-solid recuperator exchanging heat between cold and hot particles

The recuperator is a counter flow heat exchanger with multiple tubes (Fig. 2.3). Radiation dominates heat transfer at high temperatures within the recuperator [36]. Hot stream

particles from solar receiver 2 enter the recuperator and fall through vertical tubes. Cold stream particles from the water splitting reactor enter and move upward using a screw drive around the tubes. The vertical tubes are filled with particles and therefore the particle flow in and out is equal to cycle flow rate. Recuperator effectiveness increases at lower flow rates as the residence time increases for a given surface area. The radiation heat transfer rate ($\dot{q}_r$) between hot (T_h) and cold stream (T_c) particles is given in Eq. 2.11 and represents heat transfer for every one-degree change in hot stream and cold stream particles with the summation equal to $\dot{Q}_r$ in Eq. 2.12.

$$\dot{q}_r = \sigma \cdot A_t \cdot (T_h^4 - T_c^4) \tag{2.11}$$

The total heat transfer rate ($\dot{Q}_r$) in Eq. 2.12 increases with recuperator effectiveness because the inlet and outlet temperatures are constant. Heat capacity ($\dot{C}_r$) is assumed equivalent for each stream and is calculated as the average of specific heats for the two inlet streams in Eq. 2.13.

$$\dot{Q}_r = \varepsilon_r \cdot \dot{C}_r \cdot (T_6 - T_9) \tag{2.12}$$

$$\dot{C}_r = \dot{n}_p \cdot \frac{1}{2} \cdot (c_{p,6} + c_{p,9}) \tag{2.13}$$

Steam generator: The steam generator further cools particles to the target water splitting temperature and uses recovered heat to generate steam for hydrogen production within the water splitting reactor and electricity production in the organic Rankine cycle. Figure 2.4 is a conceptual schematic of the steam generator showing three subcomponents: (i) an economizer to heat water from room temperature to saturation temperature, (ii) an evaporator to generate steam, and (iii) a superheater to increase steam temperature to the target water splitting temperature. The quantity of water supplied to the steam generator depends on the inlet and exit temperatures of the particles and desired steam temperature.

Water flow rate updates dynamically to maintain the steam generator energy balance with respect to changes in particle flow rate that vary in accordance with solar insolation levels.

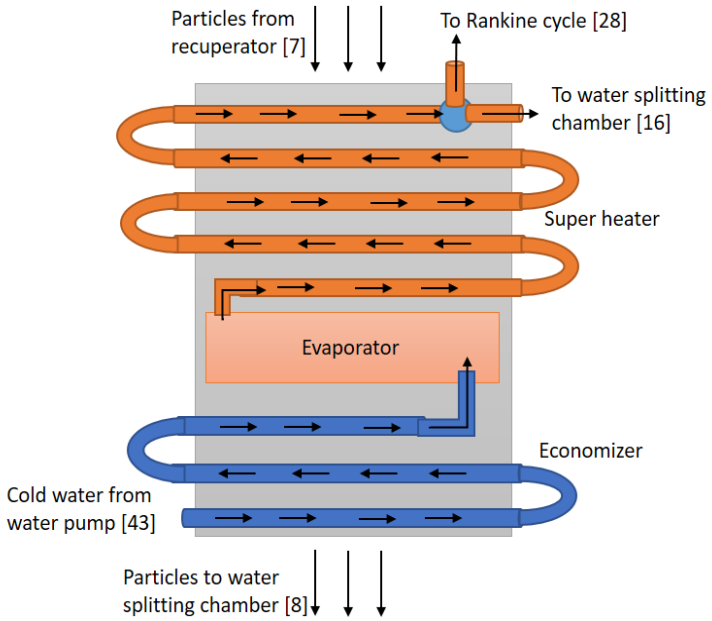

Figure 2.4. Steam generator internal design with water (blue) and steam (orange)

The total heat transfer in steam generator ($\dot{Q}_{sg}$) is calculated using Eq. 2.14 with the water flow rate ($\dot{n}_{43}$) calculated from Eqs. 2.15-2.17 where Q_{ec} is the amount of heat (J/mol) required to raise a mole of water from room temperature to a saturated liquid, and Q_{sh} is amount of heat required to raise a mole of saturated steam to the target water splitting temperature (T_{16}).

$$\dot{Q}_{sg} = n_7 \cdot \left(\frac{c_{p,7}+c_{p,8}}{2}\right) \cdot (T_7 - T_8) \tag{2.14}$$

$$\dot{n}_{43} = \frac{\dot{Q}_{sg}}{Q_{ec}+Q_{lat}+Q_{sh}} \tag{2.15}$$

$$Q_{ec} = \left(\frac{c_{p,43}+c_{w,sat}}{2}\right) \cdot (T_{sat} - T_{43}) \tag{2.16}$$

$$Q_{sh} = \left(\frac{c_{s,sat}+c_{p,16}}{2}\right) \cdot (T_{16} - T_{sat}) \tag{2.17}$$

Water splitting reactor: Particles and superheated steam come into direct contact within the water splitting reactor (Fig. 2.5). Streams flow countercurrent to maximize reaction progression by avoiding contact between re-oxidized particles and produced hydrogen. This also maintains a steam stream oxygen partial pressure that is more than the vapor pressure of the oxygen in particles. Particles re-oxidize and approach thermodynamic equilibrium but do not complete the reaction because of anticipated kinetic limitations not described in this work. Excess steam (ζ) in is supplied to meet anticipated reaction kinetics using a theoretical minimum flow rate (ζ_{min}) and a controllable excess steam factor (α) in Eq. 2.20. Water splitting is governed by energy conservation in Eq. 2.18, mass conservation in Eq. 2.19, excess steam in Eq. 2.20 and Eq. 2.21, re-oxidation effectiveness in Eq. 2.22 and re-oxidation effectiveness (ε_o) in Eq. 2.23. Re-oxidation effectiveness is the ratio between reduction and actual re-oxidation extents to that of reduction and equilibrium re-oxidation extents, with δ_{ox} as the actual reduction extent after re-oxidation and δ_{ox}^{eq} is the equilibrium reduction extent after re-oxidation of particles at their exiting temperature and the oxygen partial pressure in the incoming gas stream. Here, y_{17} is defined as the ratio of H_2 to H_2O+H_2 in the water splitting reactor exiting stream and $p_{O_2,16}$ is the oxygen partial pressure in steam entering the water splitting reactor.

$$\dot{E}_8(T_8, \delta_R) - \dot{E}_9(T_9, \delta_{ox}) = \dot{E}_{17}(T_{17}, y_{17}) - \dot{E}_{16}(T_{16}) - \dot{Q}_{22} \tag{2.18}$$

$$\dot{n}_g \cdot y_{17} = \dot{n}_p \cdot (\delta_6 - \delta_9) \tag{2.19}$$

$$\zeta = \frac{\zeta_{min}}{\alpha} \tag{2.20}$$

$$\dot{n}_g = \varepsilon_o \cdot \delta_R \cdot (\zeta + 1) \cdot \dot{n}_p \tag{2.21}$$

$$\delta_{ox} \equiv \delta_9 = (1 - \varepsilon_o)\delta_R + \varepsilon_o \delta_{ox}^{eq}(T_9, p_{O_2,16}) \tag{2.22}$$

$$\varepsilon_o = \frac{\delta_R - \delta_{ox}}{\delta_R - \delta_{ox}^{eq}} \tag{2.23}$$

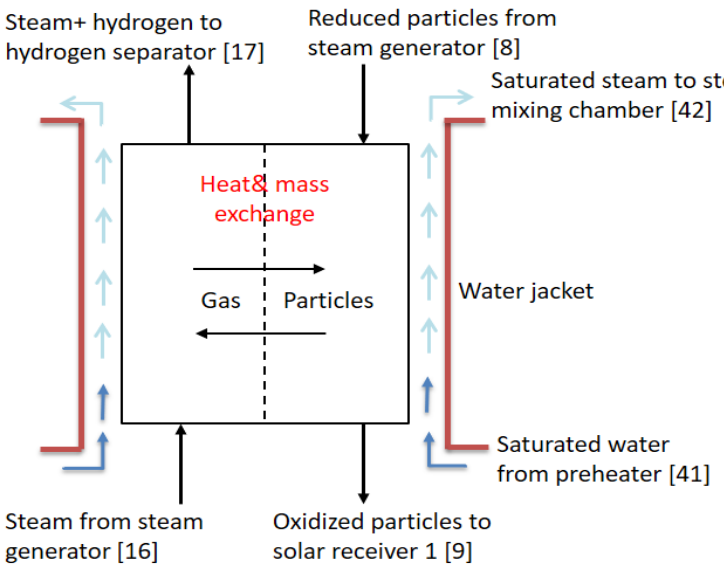

Figure 2.5. Water splitting reactor with cooling system showing countercurrent flow with heat and mass exchange

The quantity of heat removed from the water splitting reactor due to the exothermic re-oxidation reaction is an adjustable model parameter, λ_0. The remaining exothermic heat $(1 - \lambda_0)$ is distributed between the gas and particles according to a maximum entropy principle in which energy distribution happens such that the net entropy change is maximized subject to energy and mass constraints.

As shown in Fig. 2.5, the water splitting reactor is cooled to utilize exothermic heat release during the re-oxidation process and to run the re-oxidation reaction at near isothermal conditions. To maintain the reaction at a nearly constant temperature, the exothermic heat produced during re-oxidation must be continuously removed at the same rate as heat release. Water at the saturated temperature, which is ready to boil, is supplied to the water splitting reactor's cooling jacket such that it immediately starts boiling. The

purpose of boiling water during reactor cooling is the expectation of high heat transfer rates during boiling. An external heat source is used to heat water from room temperature to saturated liquid temperature. The water flow rate for the water splitting reactor cooling is calculated using Eq. 2.24.

$$\dot{n}_{40} = \frac{\lambda_0 \cdot \dot{Q}_{ext}}{Q_{lat}} \tag{2.24}$$

Preheater: Electrical energy is used to preheat water from room temperature to near boiling before being sent to cool the water splitting reactor. Electrical energy supplied to the preheater ($\dot{Q}_{38}$) is calculated as given in Eq. 2.25.

$$\dot{W}_{34} = \frac{\dot{n}_{40} \cdot (\frac{c_{p,40} + c_{p,41}}{2}) \cdot (T_{41} - T_{40})}{\eta_{e-h}} \tag{2.25}$$

Solid particle elevator: The elevator transports re-oxidized particles from the water splitting reactor to solar receiver 1 with the work requirement ($\dot{W}_{29}$) given in Eq. 2.26.

$$\dot{W}_{29} = \frac{\dot{m}_p \cdot g \cdot h_{elv}}{\eta_{elv}} \cdot \frac{1}{\eta_{e-m}} \tag{2.26}$$

Heat exchangers: Heat exchangers cool the two oxygen streams exiting the solar receivers to reduce vacuum pump work load. The flow rate of cooling water is dynamically adjusted to maintain an exiting oxygen temperature that is near atmospheric temperature, subject to a constraint that the water should not boil. The logarithmic mean temperature difference (LMTD) method is used for heat exchanger energy and mass balance calculations given that the inlet and outlet temperatures of both the cold and hot streams are known.

Vacuum pumps 1 and 2: Low oxygen partial pressure is maintained using a vacuum pump for each receiver that continuously removes oxygen as expressed in Eq. 2.27 and Eq. 2.28.

$$\dot{W}_{30} = \frac{\dot{n}_{19} \cdot \mathrm{R} \cdot T_{19} \cdot \mathrm{Ln}(P_{r,vp1})}{\eta_{vp1}} \cdot \frac{1}{\eta_{e-m}} \tag{2.27}$$

$$\dot{W}_{31} = \frac{\dot{n}_{15} \cdot \mathrm{R} \cdot T_{15} \cdot \mathrm{Ln}(P_{r,vp2})}{\eta_{vp2}} \cdot \frac{1}{\eta_{e-m}} \tag{2.28}$$

Steam mixing chamber: Steam at different temperatures is mixed before being sent to the condensing process in the hydrogen separator that delivers excess heat to the organic Rankine cycle.

Water pump: A pump introduces water to the system with a pressure rise equivalent to the total head loss of the heat exchangers, steam generator, and water splitting reactor. Piping losses are ignored. Water volumetric flow rate is calculated in Eq. 2.29 as a summation of water needs from other energy and mass balances throughout the system. Total work supplied ($\dot{W}_{33}$) to the pump is calculated in Eq. 2.30.

$$\dot{V}_w = \frac{\dot{n}_{39} \cdot M_w}{\rho_w} \tag{2.29}$$

$$\dot{W}_{33} = \frac{\rho_{wat} \cdot g \cdot H_{loss} \cdot \dot{V}_w}{\eta_{wp}} \cdot \frac{1}{\eta_{e-m}} \tag{2.30}$$

Steam pump: A pump transfers steam into the steam mixing chamber with work ($\dot{W}_{35}$) expressed in Eq. 2.31.

$$\dot{W}_{35} = \frac{\dot{n}_{22} \cdot \mathrm{R} \cdot T_{22} \cdot \mathrm{Ln}(P_{r,sp})}{\eta_{sp}} \cdot \frac{1}{\eta_{e-m}} \tag{2.31}$$

Hydrogen pump: A pump transfers hydrogen into a storage tank with work ($\dot{W}_{32}$) expressed in Eq. 2.32.

$$\dot{W}_{32} = \frac{\dot{n}_{26} \cdot \mathrm{R} \cdot T_{26} \cdot \mathrm{Ln}(P_{r,hp})}{\eta_{hp}} \cdot \frac{1}{\eta_{e-m}} \tag{2.32}$$

Hydrogen separator: Hydrogen is separated from the steam-hydrogen mixture by condensing steam. Waste heat from this process is collected and transferred to a boiler component of a simple organic Rankine cycle. Heat transferred through the hydrogen

separator ($\dot{Q}_{hs}$) includes the sensible heat of hydrogen, sensible heat of superheated steam, latent heat of water, and sensible heat of water as shown in Eq. 2.33.

$$\dot{Q}_{hs} = \dot{E}_{17} + \dot{E}_{24} - \dot{E}_{25} - \dot{E}_{26} \tag{2.33}$$

2.3.2 Electricity Coproduction Sub-system

An organic Rankine cycle utilizes reject heat from the hydrogen separator to generate electrical power and improve system efficiency. The hydrogen separator of the hydrogen production sub-system acts as a boiler in the organic Rankine cycle. Toluene, cyclohexane, and siloxane D4 are the three organic fluids compatible with this cycle [45]. A screw expander turbine is used to provide better energy conversion efficiency [38]. Mechanical work ($\dot{W}_t$) from the turbine is given in Eq. 2.34 and converted into electrical power ($\dot{W}_e$) in Eq. 2.35. Internal electrical work consumption ($\dot{W}_{aux}$) for pumps, preheater and the elevator are given in Eq. 2.36. The difference between the generated electrical power and auxiliary power consumption expresses the net electrical work ($\dot{W}_{net}$) in Eq. 2.37.

$$\dot{W}_t = \eta_R \cdot \dot{Q}_{hs} \tag{2.34}$$

$$\dot{W}_e = \eta_{gen} \cdot \dot{W}_t \tag{2.35}$$

$$\dot{W}_{aux} = \dot{W}_{29} + \dot{W}_{30} + \dot{W}_{31} + \dot{W}_{32} + \dot{W}_{33} + \dot{W}_{34} + \dot{W}_{35} \tag{2.36}$$

$$\dot{W}_{net} = \dot{W}_e - \dot{W}_{aux} \tag{2.37}$$

2.3.3 Performance Metrics

The hydrogen production rate ($\dot{n}_{H2}$) is the product of the aggregate hydrogen-steam flow rate exiting water splitting reactor and the hydrogen fraction.

$$\dot{n}_{H2} = y_{17} \cdot \dot{n}_{17} \tag{2.38}$$

$$y_{17} = \frac{\dot{n}_{H2}}{\dot{n}_{H2}+\dot{n}_{H2O}} \tag{2.39}$$

System efficiency (η_{sys}) is expressed as the ratio of the combined hydrogen and electrical output rate to the total heat input rate to the system as given in Eq. 2.40. Hydrogen energy is calculated using Gibbs free energy (ΔG) to be consistent with electrical energy expressed as exergy. Annual average system efficiency is the ratio of total energy output in one year (E_{annual}) to the total solar heat input in one year (Q_{annual}) as given in Eq. 2.41 using actual hourly solar DNI data to calculate $\dot{Q}_1$ and simulate energy output.

$$\eta_{sys} = \frac{\dot{n}_{H2} \cdot (\Delta G) + \dot{W}_{net}}{\dot{Q}_1} \tag{2.40}$$

$$\eta_a = \frac{E_{annual}}{Q_{annual}} \tag{2.41}$$

The instantaneous receiver-to-hydrogen efficiency is expressed as the ratio of the hydrogen energy output rate to the total heat input rate to the system in Eq. 2.42, with the receiver-to-electrical efficiency expressed as the ratio of the electrical energy rate output to the total heat input to the system in Eq. 2.43. The receiver-to-hydrogen efficiency is calculated based on HHV to permit comparison with similar formulations used in existing literature.

$$\eta_h = \frac{\dot{n}_{H_2} \cdot HHV}{\dot{Q}_1} \tag{2.42}$$

$$\eta_e = \frac{\dot{W}_{net}}{\dot{Q}_1} \tag{2.43}$$

2.4. Simulation procedure and Input Parameters

Table 1.1 and Table 1.2 show design point parameters and model baseline inputs for the design point simulation at 900 W/m^2 DNI, respectively. It is assumed for simplicity that both emissivity and absorptivity of the solar receivers are equal to one. The sensitivity of design parameters including recuperator effectiveness, partial pressure of oxygen in the receivers, excess steam factor, and re-oxidation effectiveness is discussed in section 5.3.

Particle flow rate decreases as DNI decreases to maintain a consistent particle outlet condition. The reduced particle flow rate increases recuperator effectiveness. An upper limit on effectiveness is fixed so that there is sufficient heat remaining in the particles at state 7 to generate the required quantity of steam at target temperature for hydrogen production. The increase in recuperator effectiveness at lower DNI leads to lower particle temperatures entering the steam generator, and hence the particle exiting temperature from the steam generator is reduced from 1250 K for DNI above 500 W/m^2 to 1150 K for DNI below 500 W/m^2 to maintain a sufficient supply of steam generation entering the water-splitting reactor. The steam temperature for water-splitting is 90% of particle temperature to run the reaction at near isothermal condition by continuously extracting the exotherm released during re-oxidation.

Pressure rise in the water pump accounts for pressure losses in heat exchangers, secondary concentrators, and steam generator, with pressure losses in heat exchangers being 50% of the entrance pressure as approximated based by heat exchanger surface area.

Table 2.1. Design point parameters

Component	Parameter	Value	Unit
Solar receivers	Partial pressure of oxygen in solar receiver 1	100	Pa
	Partial pressure of oxygen in solar receiver 2	10	Pa
	Target reduction temperature [9]	1773	K
Solid-solid recuperator	Effectiveness [47]	0.7	-

Table 2.2. Baseline model input parameters

Component	Parameter	Value	Unit
Water-splitting chamber	Re-oxidation effectiveness (ε_o)	0.90	-
	Excess steam factor (α)	0.60	-
	Fraction of exothermic heat expelled (λ_0)	0.99	-
	Particles entering temperature (T_8)		
	(DNI > 500 W/m^2)	1250	K
	(DNI ≤ 500 W/m^2)	1150	K
	Steam entering temperature (T_{16})		
	at DNI > 500 W/m^2)	1125	K
	at DNI ≤ 500 W/m^2)	1035	K
Solid particle elevator	Elevator height	20	M
	Mechanical conversion efficiency	70	%
Organic Rankine cycle	Heat to mechanical conversion efficiency	40	%
	Mechanical to electrical conversion efficiency	98	%
Pumps	Electrical to mechanical conversion efficiency	85	%

Ambient conditions are 298.15 K and 101.325 kPa for the air temperature and pressure, respectively, with 21.2235 kPa for ambient oxygen partial pressure. Annual performance metrics are calculated using TMY3 solar radiation data from Daggett [46] and a constant solar field efficiency of 45%.

2.5. Results and Analysis

2.5.1 Design Point Simulation

Stream flows and state point values for the complete system are given in Table 2 for a design point simulation at 900 W/m^2 DNI. Enthalpy values of water and steam use a

reference point of 273.15 K and ambient pressure with oxygen and hydrogen as absolute values. Pressure in streams 14, 15, 18, and 19 represent oxygen partial pressure whereas the remaining streams indicate total stream pressure. The enthalpy values are determined from the properties of ceria using fitting parameters to data in the literature [55]. Hydrogen production is 23.42 mol/s with exiting oxygen at streams 15 and 18 summing to 11.71 mol/s. Make-up water is added to the system to maintain overall mass balance. The temperature of stream 5 is calculated such that the solar radiation input or concentration ratio of both the stages is approximately same.

External heat and work rates are given in Table 3. A total of 27.74 MW solar radiation is supplied to the system at states 2, 3, and 4. Losses from solar stage 2 are 17.36% higher than solar stage 1 due to the increased average temperature of solar stage 2. Electrical power use for auxiliary loads (streams 29-34) consumes 21.96% of total electricity generated (steam 44).

Table 4 enumerates excess in the system that is not used for hydrogen production. Total excess heat equates to 21.89 MW, of which 4.19 MW (19.14%) are radiation losses that cannot be recovered and the remaining 17.70 MW (80.85%) is captured and supplied to the organic Rankine cycle for electricity production.

The oxygen volumetric flow rates at the design point from stage 1 and 2 are 2920 m^3/s and 9329 m^3/s. The oxygen pumping speeds at design point from stage 1 and 2 assuming curtain area is 10 times the aperture area are 62 m/s and 198 m/s [34], [53]. The maximum pumping speed is 229 m/s at maximum DNI 1041 W/m^2. The oxygen pumping speed at any DNI is less than sonic speed in oxygen (800 m/s at 1773 K) [34]. Receiver

design, number of stages, and windows per stage could be optimized to further reduce pumping speeds.

Table 2.3. State values for stream flows

State	Energy flow (MW)	Matter flow rate (mol/s)	Temperature (K)	Pressure (Pa)	Enthalpy (J/mol)	Specific heat (J/mol-K)
5	269.07	859.20	1,705		313,150	82.83
6	279.24	859.20	1,773		324,982	83.17
7	253.37	859.20	1,404		294,884	81.03
8	242.80	859.20	1,250		282,578	79.8
9	232.63	859.20	1,245		270,744	79.76
10	258.49	859.20	1,635		300,842	82.46
11	258.49	859.20	1,635		300,842	82.46
12	0.10	34.48	298	1,470,000	1,912	75.29
13	0.42	34.48	435	647,262	12,316	78.25
14	0.33	6.45	1,773	10	50,682	37.38
15	0.00	6.45	300	10	62.32	29.37
16	5.02	65.04	1,125	101,000	77,143	42.87
17	10.82	65.04	1,254	101,000	166,168	39.69
18	0.25	5.26	1,705	25	48,136	37.21
19	0.00	5.26	300	25	62.32	29.37
20	0.05	26.66	298	1,470,000	1,912	75.29
21	0.30	26.66	435	647,262	12,316	78.25
22	3.02	61.14	440	323,631	49,316	38.02
23	3.08	61.14	440	355,994	50,311	38.41
24	14.06	238.90	609	101,000	56,278	38.6
25	0.53	280.50	298	101,325	1,889	75.36
26	6.69	23.42	298	101,325	293,756	28.84
27	6.69	23.42	298	2,170,000	293,774	28.95
28	5.81	69.21	1,125	101,000	77,070	43.03
39	0.58	304.00	298	1,470,000	1,912	75.29
40	0.21	108.60	298	1,470,000	1,912	75.29
5	269.07	859.20	1,705		313,150	82.83
6	279.24	859.20	1,773		324,982	83.17
7	253.37	859.20	1,404		294,884	81.03

Table 2.4. External heat and work rates at design point DNI

State	Heat rate (MW)	State	Work rate (MW)
1	63.93	29	0.04
2	12.73	30	0.15
3	12.72	31	0.36
4	2.29	32	0.25
36	36.18	33	0.01
37	1.93	34	0.61
38	2.26	35	0.06
45	10.72	44	6.93

Table 2.5. Excess heat in the system

Component	Heat rate (MW)	Part of total (%)	Utilization
Steam generator	10.57	48.31	Recovered
Water-splitting reactor	4.32	19.74	Recovered
Secondary concentrators	2.29	10.45	Recovered
Solar receiver 2	2.23	10.19	Lost
Solar receiver 1	1.90	8.67	Lost
Heat exchanger 2	0.33	1.49	Recovered
Heat exchanger 1	0.25	1.15	Recovered
Total	**21.92**	**100.00**	

Performance metrics are summarized in Table 5 for the design point DNI. A solar radiation input of 27.74 MW into the solar stages produces a total of 10.96 MW comprised of 5.55 MW hydrogen energy (based on Gibbs free energy) and 5.41 MW of electrical energy. System efficiency equates to 39.52%. The hydrogen energy output rate is 6.69 MW using HHV for comparison with other literature. The receiver-to-hydrogen factor and electrical factor are given in Table 2.6.

Table 2.6. Design point performance metrics

Variable	Value	Unit
Reduction extent	0.031	-
Oxidation extent	0.003	-
H_2/(H_2O+H2) ratio (y_{17})	0.360	-
Water-splitting reactor H_2+H_2O exit flow rate	65.04	mol/s
Hydrogen production rate	23.42	mol/s
Oxygen flow rate from solar stage 1	5.26	mol/s
Oxygen flow rate from solar stage 2	6.45	mol/s
Water-splitting reactor exotherm	4.39	MW
Total electricity generation	6.92	MW
Net electricity generation (after auxiliary loads)	5.41	MW
Hydrogen energy production rate (HHV)	6.69	MW
Hydrogen energy production rate (ΔG^0)	5.55	MW
Auxiliary power consumption	1.52	MW
System efficiency	39.52	%
Receiver-to-hydrogen factor (ΔG^0)	50.7	%
Receiver-to-electrical factor	49.3	%

2.5.2 Annual Performance

Annual performance metrics in Table 2.7 are calculated using hourly DNI values across the simulated year. The annual average receiver-to-hydrogen efficiency is higher than design point because efficiency increases at lower DNI values as recuperator effectiveness increases, which also causes the annual average receiver-to-electrical efficiency to be lower than the design point because less heat is recovered for electricity generation. The combined effect of these two efficiencies is reflected in annual average system efficiency that is less than the design point.

Table 2.7. Annual performance metrics

Variable	Value	Unit
Heat input to the system	83.00	GWh/year
Hydrogen production (HHV)	20.45	GWh/year
Hydrogen production (Gibbs)	16.96	GWh/year
Net electricity generation	14.60	GWh/year
Hydrogen production per year	515.14	tonne
System efficiency	38.03	%
Receiver-to-hydrogen (HHV)	24.64	%
Receiver-to-hydrogen (Gibbs)	20.44	%
Receiver-to-electrical	17.59	%

2.5.3 Sensitivity Analysis

Sensitivity analysis was used to evaluate the effect of DNI, recuperator effectiveness, oxygen partial pressures in the solar stages, particle re-oxidation temperature, re-oxidation effectiveness, and excess steam factor on performance metrics measured on both an instantaneous basis and an annual basis.

System efficiency holds relatively steady between 37.94% and 40.59% as the nominal recuperator effectiveness is increased from 0.3 to 0.8 in Fig 6. The receiver-to-electrical contribution decreases and receiver-to-hydrogen contribution increases with increasing recuperator effectiveness because more waste heat is kept within the hydrogen production loop. The rise in hydrogen contribution is greater than the drop in electrical contribution and hence total system efficiency increases modestly with increasing recuperator effectiveness.

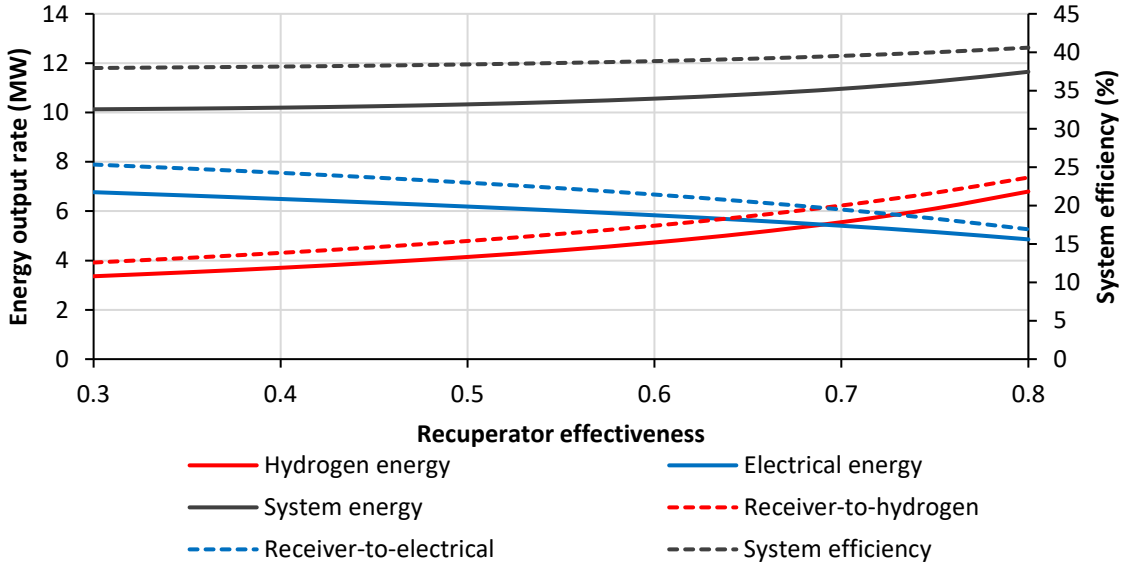

Figure 6. Energy output and efficiency with varying recuperator effectiveness at a constant DNI of 900 W/m^2

Unlike thermochemical systems without co-generation [61], overall system efficiency does not significantly vary with changing recuperator effectiveness as shown in Fig. 6 and further elucidated in Fig. 7. An average 1.9% relative difference is observed in system efficiency with recuperator effectiveness varied between 0.3 and 0.8 across a DNI range of 300 to 1000 W/m^2.The average difference in receiver-to-hydrogen fraction is 22.3%. The shape of the curves in Fig. 7 shifts at 500 W/m^2 DNI because the re-oxidation

temperature of particles changes from 1150 K to 1250 K to maintain sufficient steam generation for water-splitting at lower DNI.

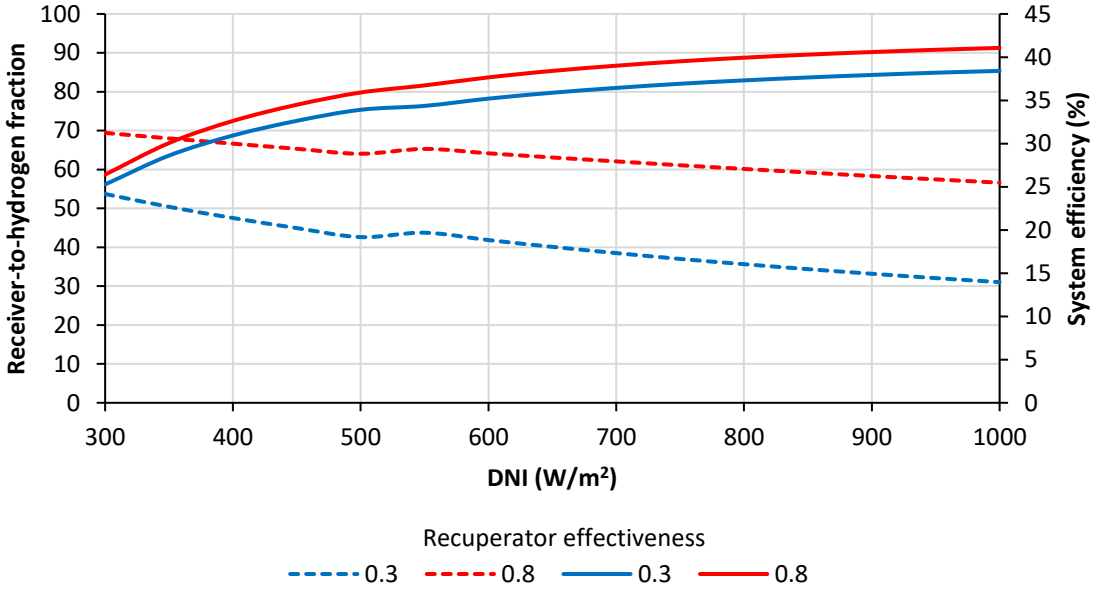

Figure 7. Effect of DNI and nominal recuperator effectiveness on instantaneous efficiency performance metrics

Figure 8 shows how heat recovery improves system efficiency. The increase in efficiency from recovering heat from secondary concentrators and the exotherm is uniform throughout the DNI range. System efficiency increases at greater DNI levels from particle sensible heat recuperation because the recuperator effectiveness decreases and permits more electricity to be generated.

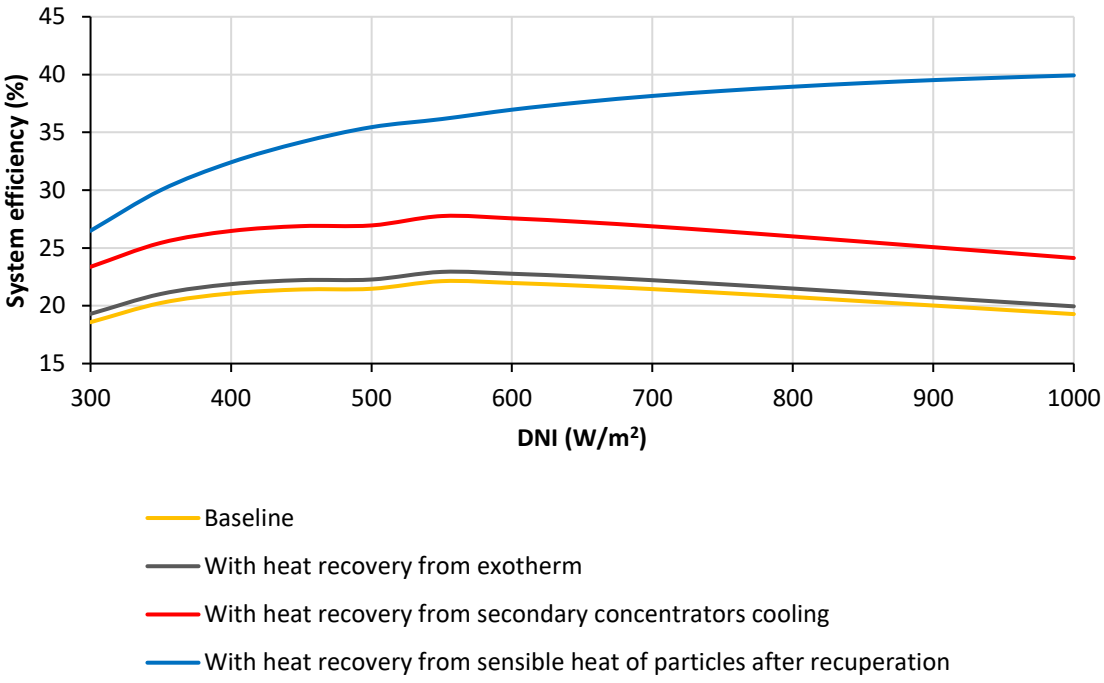

Figure 8. Instantaneous system efficiency with different heat recovery options

Annual average system efficiency is sensitive to recuperator effectiveness and the oxygen partial pressure in solar stages as shown in Fig. 9. The oxygen partial pressure in solar stage 1 is held at 10 times that of solar stage 2 for each case considered. System efficiency increases from 36.50% to 39.08% (2.58% change) for an increase in recuperator effectiveness from 0.3 to 0.8, respectively, at an oxygen partial pressure of 10 Pa, which is more significant than the increase in system efficiency from 34.88% to 35.00% (0.12% change) over the same recuperator effectiveness range for an oxygen partial pressure of 10,000 Pa. This occurs because the particle extent of reduction is higher at lower oxygen partial pressures.

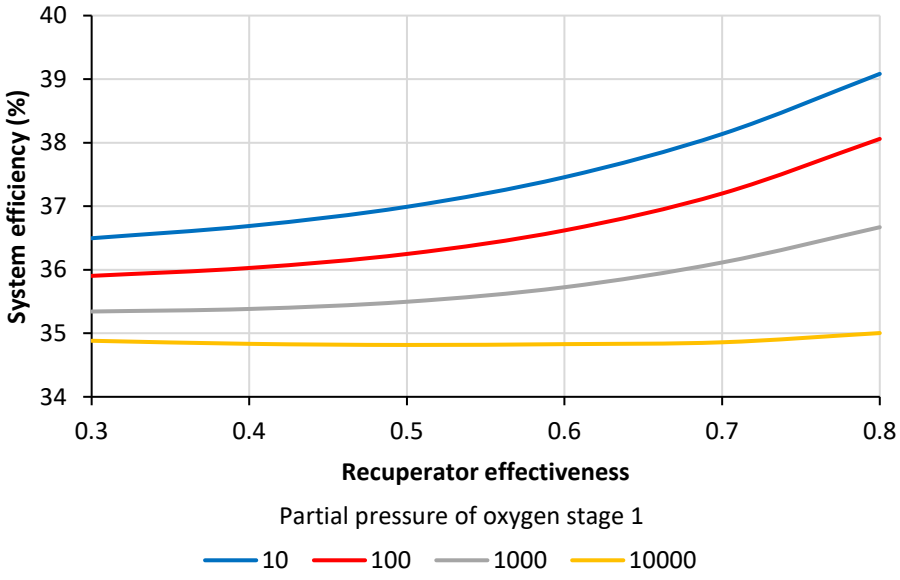

Figure 9. Annual average system efficiency for varying recuperator effectiveness and solar stage oxygen partial pressure

Figure 10 shows that the annual average hydrogen energy (ΔG^0) is relatively independent of the excess steam factor, indicating that more steam can be supplied to the water-splitting reactor without affecting hydrogen production. But excess steam is supplied to water-splitting reactor anticipating better reaction kinetics. However, the re-oxidation reaction effectiveness significantly affects hydrogen production.

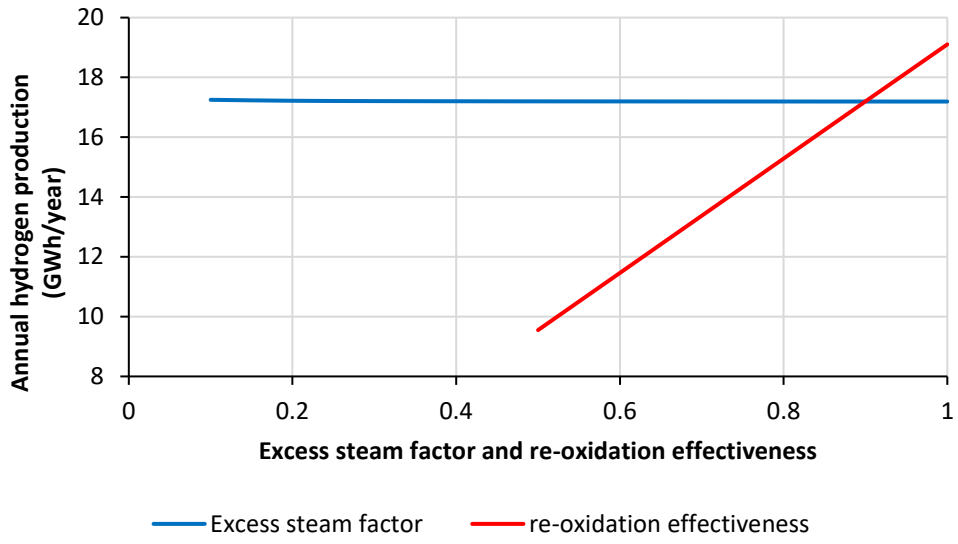

Figure 10. Annual average receiver-to-hydrogen efficiency for varying excess steam factor and re-oxidation effectiveness

2.6. Discussion

Results introduce and demonstrate a solar thermochemical water-splitting process coupled to an organic Rankine cycle to produce electricity and improve system efficiency beyond that achieved using other approaches. The thermodynamic model was demonstrated with ceria but kept generic for use with other redox-active material by permitting the design parameters and operating points to be adjusted for optimal operation. Two compound solar receivers (stages) were used to bring the oxygen partial pressure to 10 Pa and particle temperature to 1773 K to achieve a reduction extent of 0.031 in ceria. The total solar radiation input to the system at the design point (DNI is 900 W/m^2) is 27.74 MW and output comprises 5.55 MW hydrogen energy (Gibbs free energy) and 5.41 MW of electrical energy and a total of 10.96 MW. The system efficiency is 39.52%

at the design point and . The annual average system efficiency was 38.14% with hydrogen efficiency (Gibbs free energy) and electrical efficiency being 20.68% and 17.46%, respectively. Total annual solar radiation energy input to the system is 83.18 GWh/year and system produces 17.20 GWh/year of hydrogen energy (Gibbs free energy) and 14.52/year GWh of electrical energy. The annual hydrogen energy produced on HHV basis is 20.73 GWh/year.

Particle recuperator effectiveness had a significant effect on hydrogen production and receiver-to-hydrogen efficiency but only a minor effect on total system efficiency because most of the waste heat was captured for electricity production. Total excess heat (heat not used for the splitting reaction) in the system is 21.89 MW at the design point, of which 17.70 MW (80.85%) is recovered from the steam generator, water-splitting reactor, hydrogen separator, and oxygen stream heat exchangers and transferred to the organic Rankine cycle.

Output and findings from this paper provide practical insights into plant design and optimal performance characteristics for hydrogen and electricity production. Future work can incorporate economic analyses to optimize component sizing and state values to minimize the cost of hydrogen and electricity production.

Acknowledgements

This material is based up on work supported by the U.S. Department of Energy, Office of Energy Efficiency and Renewable Energy (EERE), specifically the Fuel Cell Technologies Office. Sandia National Laboratories is a multi-mission laboratory managed and operated by National Technology and Engineering Solutions of Sandia LLC, a wholly owned

subsidiary of Honeywell International Inc., for the U.S. Department of Energy's National Nuclear Security Administration under contract DE-NA0003525

CHAPTER 3

TECHNO-ECONOMIC ANALYSIS OF THERMOCHEMICAL WATER-SPLITTING SYSTEM FOR CO-PRODUCTION OF HYDROGEN AND ELECTRICITY

In preparation for submission to *Solar Energy* journal

Abstract- This study is estimate the cost to produce one kg of hydrogen in a 30 MW solar thermochemical water-splitting reactor with electricity co-production. The work includes individual component sizing based on total energy conversion in each component and factors affecting size and performance of the component. The multi tubular recuperator size is 209 m^2 to exchange 26 MW of heat through thermal radiation between the hot and cold stream particles. Hydrogen separator size is calculated assuming steam and hydrogen reject heat separately and then summation gives total area. The hydrogen separator is 570 m^2 to exchange 17.5 MW of heat between hydrogen+steam and working fluid of organic Rankine cycle. The size of the steam generator and hydrogen separator can be reduced by increasing the inlet water pressure up to 20 bar. Total annual capital expenditure is estimated based on component cost, maintenance cost and revenue from electricity generation based on annual average performance. The cost to produce one kg of hydrogen from this system is estimated as $4.40 assuming 25 years plant life. Improving recuperator effectiveness from 0.7 to 0.8 is a high-value design modification resulting in a 12% decrease in hydrogen cost for a modest 2% increase in plant cost.

3.1. Introduction

Concentrations of greenhouse gases such as carbon dioxide, sulfur dioxide, nitrogen oxide, and carbon monoxide are expected to increase given rising global energy demand, with hydrocarbons expected to be a significant source of primary energy for decades to come [1]–[3]. Hydrogen can displace traditional hydrocarbon fuels in internal combustion engines and enable alternative energy source in vehicles such as fuel cells with high efficiency and low emissions [4]–[7]. Production of large quantities of hydrogen at low-cost remains an area for much research [8], [9]. Conventional methods to produce hydrogen from fossil fuels yield carbon emissions [10], and the electrolysis is energy intensive and may also generate emissions if electricity is produced from fossil fuels [11]. These conventional practices are not expected to meet the growing demand for hydrogen, at low-cost, and at a sufficient scale for global transportation needs [4]. New methods that use concentrating solar energy to power electrochemical or thermochemical reactions are an alternative that is beginning to show promise to create lower cost, sustainable, clean burning fuels [12]. One such solution uses a two-step thermochemical water-splitting process with a combination of reduction and re-oxidation chemical reactions for producing hydrogen fuel [13]–[17]. Early work with metal oxides of Iron, Cadmium, Germanium and Zinc were extensively studied for thermochemical water-splitting but these materials are limiting due to their physical and chemical properties like melting point and reduction temperature [18]–[24]. Oxides of cerium introduced by Abanades in 2006 continue to be the preferred material for thermochemical water-splitting because Ceria is stable at high temperatures, doesn’t need quenching and has rapid fuel production kinetics [17], [22], [25]–[27].

The efficiency of thermochemical water-splitting laboratory scale reactor using ceria as metal oxide is up to 30% with parameters partial pressure of oxygen in stage as 1 Pa and 50% heat recuperation from particles [15], [28]–[30]. In a large scale 30 MW plant, the system efficiency is up to 40% for combined co-production of hydrogen and electricity using ceria as metal oxide. Multiple stages with cascading pressure reduction is used in MW scale plant where oxygen partial pressure decreases from 25 Pa to 10 Pa in multiple stages or stages.

This work advances prior science with applied research for system sizing and balance of plant cost estimation. Components are right-sized to meet energy conversion requirements with sensitivity analysis performed to reduce costs subject to minimum hydrogen production targets. A recuperator design for particle-particle heat exchange is proposed with a detailed thermodynamic analysis completed to explore the effect of various design features that affect size component size. The sizes of steam generator to extract excess heat from particles and hydrogen separator to separate hydrogen from steam are calculated in this model. The cost to produce hydrogen is estimated from the size and cost of all components including finance and maintenance costs for the plant with a 25-year lifetime.

3.2. System Description

The thermochemical water-splitting system shown in Fig. 3.1 is comprised of two subsystems for hydrogen production and electricity production with a total of 23

components and 45 stream states in the full system. Governing equations of each component are given in Table 3.1 with summary descriptions following.

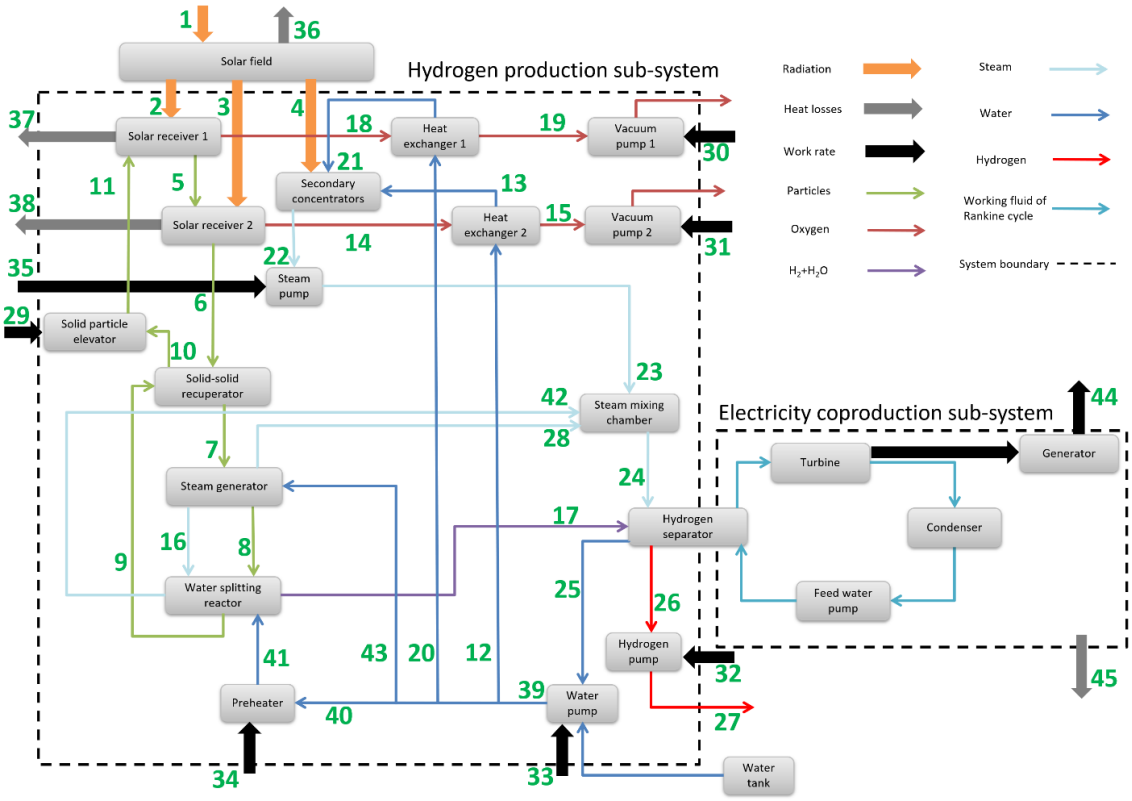

Figure 3.1. Component diagram of solar thermochemical co-production of hydrogen and electricity

Two solar receivers absorb heat from the solar field and act as thermal reduction chambers with particles heated and partially reduced in the first receiver and then reduced further in the second receiver to a target extent of thermal reduction. Total particle flow rate is based on the heat available in receiver 2. Two vacuum pumps are used, one for each receiver, to maintain the required vacuum to achieve particle reduction. Two heat exchangers cool the exiting oxygen streams to reduce power consumption of the vacuum pumps since mechanical work decreases with decrease in temperature and recapture this energy to preheat steam.

After thermal reduction, particles are cooled to the optimal re-oxidation temperature using a recuperator and steam generator. The recuperator transfers heat to cold particles using thermal radiation, with slower particle flow rates increasing recuperator effectiveness [55]. Particles then enter the steam generator and are cooled to the desired re-oxidation temperature. Heat from the particles generates super-heated steam for use in the re-oxidation reaction with any excess steam used for electricity generation to increase system efficiency. Water flow rate to the steam generator varies with particle flow rate and temperature such that the super-heated steam exits at the target re-oxidation temperature.

The water-splitting reactor contains particles and steam running counter flow so that the partial pressure of oxygen in the steam is always more than vapor pressure of oxygen in particles. Particles re-oxidize and strip oxygen from steam to produce hydrogen. Re-oxidized particles are returned to the solar receivers using an elevator to begin the next cycle. Excess steam is supplied to the water-splitting reactor to ensure that full re-oxidization potential is reached before particles exit the reactor. Exotherm heat released during the re-oxidation reaction is absorbed by a cooling water jacket that enters near the saturation temperature and absorbs heat during vaporization. A mixture of steam and hydrogen exit the water-splitting reactor for future separation when steam is condensed out of the mixture. A pump is used to compress and store hydrogen at 21 bar.

The various steam flows are combined in a mixing chamber including steam from secondary concentrators, the water-splitting reactor cooling jacket, and excess steam from the steam generator. The combined steam stream is also sent through the hydrogen separator (condenser) that is used to pass excess heat from the hydrogen production sub-system to the organic Rankine cycle to produce electricity. Electricity generated in the

Rankine cycle is used to for the internal pumps and water pre-heater with any excess electricity sold to the wholesale electric market. A water pump and steam pump are used to increase stream pressure to account for losses in pipes and components.

Table 3.1. Components and governing equations

Component	Equation	Comments
Solar stage 1	$\dot{Q}_2 = \dot{E}_{18} + \dot{Q}_{19} + (\dot{n}_p \cdot (h_5 - h_{11}))$	Heat input to receiver 1
	$h_{loss} \cdot A_{SR1} \cdot \left(\frac{T_{11} + T_5}{2} - T_0\right)$	Convection losses from receiver 1
	$\sigma \cdot A_{ap1} \cdot \left(\frac{T_5^5 - T_{11}^5}{5 \cdot (T_5 - T_{11})} - T_0^4\right)$	Radiation losses from receiver 1
Solar stage 2	$\dot{Q}_3 = \dot{E}_{14} + \dot{Q}_{21} + (\dot{n}_p \cdot (h_6 - h_5))$	Heat input to receiver 2
	$h_{loss} \cdot A_{SR2} \cdot \left(\frac{T_5 + T_6}{2} - T_0\right)$	Convection losses from receiver 2
	$h_{loss} \cdot A_{SR2} \cdot \left(\frac{T_5 + T_6}{2} - T_0\right)$	Radiation losses from receiver 2
Secondary concentrators	$\dot{Q}_4 = q_{lat} \cdot (\dot{n}_{13} + \dot{n}_{21})$	Heat supplied to secondary concentrators
Recuperator	$\dot{Q}_{rec} = \varepsilon_{rec} \cdot \dot{C}_{rec} \cdot (T_6 - T_9)$	Total heat transfer
	$\dot{C}_r = \dot{n}_p \cdot \frac{1}{2} \cdot (c_{p_6} + c_{p_9})$	Heat capacity
Steam generator	$\dot{Q}_{SG} = n_7 \cdot (\frac{c_{p_7} + c_{p_8}}{2}) \cdot (T_7 - T_8)$	Sensible heat lost by particles
	$\dot{n}_{43} = \frac{\dot{Q}_{GS}}{q_{ec} + q_{lat} + q_{sh}}$	Water flow rate
	$Q_{ec} = (\frac{c_{p,43} + c_{w,sat}}{2}) \cdot (T_{sat} - T_{43})$	Sensible heat to water per mole
	$Q_{sh} = (\frac{c_{s,sat} + c_{p,16}}{2}) \cdot (T_{16} - T_{sat})$	Sensible heat to steam per mole
Pre-heater	$\dot{n}_{40} = \frac{\lambda_0 \cdot \dot{Q}_{ext}}{Q_{lat}}$	Cooling water flow rate

	$\dot{W}_{34} = \frac{\dot{n}_{40} \cdot (\frac{c_{p,40} + c_{p,41}}{2}) \cdot (T_{41} - T_{40})}{\eta_{e-h}}$	Heat input
Water-splitting reactor	$\dot{H}_8 - \dot{H}_9 = \dot{H}_{17}(\mathrm{T}_{17}, y_{17}) - \dot{H}_{16} - \dot{Q}_{22}$	Energy balance
	$\dot{n}_g \cdot y_{17} = \dot{n}_p \cdot (\delta_6 - \delta_9)$	Mass balance
	$\zeta = \frac{\zeta_{min}}{\alpha}$	Excess steam factor
	$\varepsilon_o = \frac{\delta_R - \delta_{ox}}{\delta_R - \delta_{ox}^{eq}}$	Effectiveness of re-oxidation reaction
	$\dot{n}_g = \varepsilon_o \cdot \delta_R \cdot (\zeta + 1) \cdot \dot{n}_p$	Gaseous flow
Elevator	$\dot{W}_{29} = \frac{\dot{m}_p \cdot g \cdot h_{elv}}{\eta_{elv}} \cdot \frac{1}{\eta_{e-m}}$	Work input
Hydrogen separator	$\dot{Q}_{hs} = \dot{E}_{17} + \dot{E}_{24} - \dot{E}_{25} - \dot{E}_{26}$	Heat lost by steam and hydrogen
Vacuum pump 1	$\dot{W}_{30} = \frac{\dot{n}_{19} \cdot \mathrm{R} \cdot T_{19} \cdot \mathrm{Ln}(P_{r,vp1})}{\eta_{vp1}} \cdot \frac{1}{\eta_{e-m}}$	Work input
Vacuum pump 2	$\dot{W}_{31} = \frac{\dot{n}_{15} \cdot \mathrm{R} \cdot T_{15} \cdot \mathrm{Ln}(P_{r,vp2})}{\eta_{vp2}} \cdot \frac{1}{\eta_{e-m}}$	Work input
Water pump	$\dot{V}_w = \frac{\dot{n}_{39} \cdot M_p}{\rho_w}$	Volume flow rate
	$\dot{W}_{33} = \frac{\rho_{wat} \cdot g \cdot H_{loss} \cdot \dot{V}_w}{\eta_{wp}} \cdot \frac{1}{\eta_{e-m}}$	Work input
Steam pump	$\dot{W}_{35} = \frac{\dot{n}_{22} \cdot \mathrm{R} \cdot T_{22} \cdot \mathrm{Ln}(P_{r,sp})}{\eta_{sp}} \cdot \frac{1}{\eta_{e-m}}$	Work input
Hydrogen pump	$\dot{W}_{32} = \frac{\dot{n}_{26} \cdot \mathrm{R} \cdot T_{26} \cdot \mathrm{Ln}(P_{r,hp})}{\eta_{hp}} \cdot \frac{1}{\eta_{e-m}}$	Work input
Organic Rankine cycle	$\dot{W}_t = \eta_R \cdot \dot{Q}_{hs}$	Mechanical power from turbine
	$\dot{W}_e = \eta_{gen} \cdot \dot{W}_t$	Total electrical power from generator
	$\dot{W}_{aux} = \dot{W}_{29} + \dot{W}_{30} + \dot{W}_{31} + \dot{W}_{32} + \dot{W}_{33} + \dot{W}_{34} + \dot{W}_{35}$	Auxiliary power consumption
	$\dot{W}_{net} = \dot{W}_e - \dot{W}_{aux}$	Net electrical power output

The input parameters and output power and efficiency values are given in Table 3.2 and Table 3.3. Detailed values of energy and mass for all stream values are given in appendix.

3.3. Component Sizing

Components are sized using equations in Table 3.2. Solar field size is calculated based on total heliostats area and receivers area based on aperture to total area ratio. Pump power is based on pumping efficiency and electrical to mechanical conversion efficiency. Organic Rankine cycle power rating is chosen based on the maximum electricity production rate of the cycle. Total quantity of particles required per tower is estimated from total residence time of particles in the cycle. Several components required more detailed thermodynamic evaluation including the recuperator, steam generator, hydrogen separator, and water-splitting reactor.

Table 3.2. Scaling parameters and size of the components

Component	Scaling Parameter	Size
Solar field	Solar field area	$A_{sf} = A_{sf,n} \cdot SM$
Receivers	Total receiver area	$A_{rec} = 2 \cdot A_r \cdot A_a$
Solid particle elevator	Elevator height	
Preheater	Heater power	$\dot{W}_{33} = \frac{\dot{n}_w \cdot c_{p,w} \cdot (T[41] - T[40])}{\eta_{e-h}}$
Heat exchanger 1	Surface area	$Q_{HX1} = U_{g-g} \cdot A_{HX1} \cdot LMTD_{HX1}$
Heat exchanger 2	Surface area	$Q_{HX2} = U_{g-g} \cdot A_{HX2} \cdot LMTD_{HX2}$
Vacuum pump 1	Power rating	$\dot{W}_{30} = \frac{\dot{n}_{19} \cdot \mathrm{R} \cdot T_{19} \cdot \mathrm{Ln}(P_{r,vp1})}{\eta_{vp1} \cdot \eta_{e-m}}$
Vacuum pump 2	Power rating	$\dot{W}_{31} = \frac{\dot{n}_{15} \cdot \mathrm{R} \cdot T_{15} \cdot \mathrm{Ln}(P_{r,vp2})}{\eta_{vp2} \cdot \eta_{e-m}}$
Steam pump	Power rating	$\dot{W}_{35} = \frac{\dot{n}_{22} \cdot \mathrm{R} \cdot T_{22} \cdot \mathrm{Ln}(P_{r,sp})}{\eta_{sp} \cdot \eta_{e-m}}$

Hydrogen pump	Power rating	$\dot{W}_{32} = \frac{\dot{n}_{26} \cdot \mathrm{R} \cdot T_{26} \cdot \mathrm{Ln}(P_{r,hp})}{\eta_{hp} \cdot \eta_{e-m}}$
Water pump	Power rating	$\dot{W}_{33} = \frac{\rho_{wat} \cdot g \cdot H_{loss} \cdot \dot{V}_w}{\eta_{wp} \cdot \eta_{e-m}}$
Organic Rankine cycle	Power rating	$\dot{W}_e = \eta_{gen} \cdot \eta_R \cdot \dot{Q}_{hs}$
Particles	Mass of particles	$\dot{m}_p = \dot{n}_p \cdot T_{res}$

3.3.1 Solid-solid Recuperator

A schematic of the solid-solid recuperator is shown in Fig. 3.2. Hot particles from the solar reduction chamber approach a diverging channel to separate particles that descend through tubes. Cold stream particles from the water-splitting reactor move upward by way of a screw around the heated tubes. Heat exchange is expressed as radiation given that it is the dominant form of heat transfer in particles above 1000 K that reach 1700 K maximum. Emissivity of the particles and tube wall is assumed as unity for baseline simulations and explored further using sensitivity analysis. The convection heat transfer coefficient between the wall and particles is less than 0.5 W/m^2-K and thus convection heat transfer is negligible. The summation of particle flow rates from all the tubes is equal to the particle flow rate in the cycle with the recuperator effectiveness being a function of the surface area of each tube, total number of tubes and particle residence time inside the tubes. Eq. 3.1 is used to calculate the total heat transfer area required for recuperator

$$\dot{Q}_{rec} = \frac{A_{rec} \cdot \sigma \cdot (T_h^4 - T_c^4)}{R_{rec}} \tag{3.1}$$

where $\dot{Q}_{rec}$ is total heat transfer rate in the recuperator, A_{rec} is total heat transfer area, T_h is average hot stream particles temperature and T_c is average cold stream particles temperature. With a_{rec} as the surface area of each tube, then the following relations can be written with the total number of tubes, n_{rec}.

$$A_{rec} = a_{rec} \cdot n_{rec} \tag{3.2}$$

$$\dot{q}_{rec,t} = \frac{a_{rec} \cdot \sigma \cdot (T_h^4 - T_c^4)}{R_{rec}} \tag{3.3}$$

where $\dot{q}_{rec,t}$ is heat transfer rate in each tube.

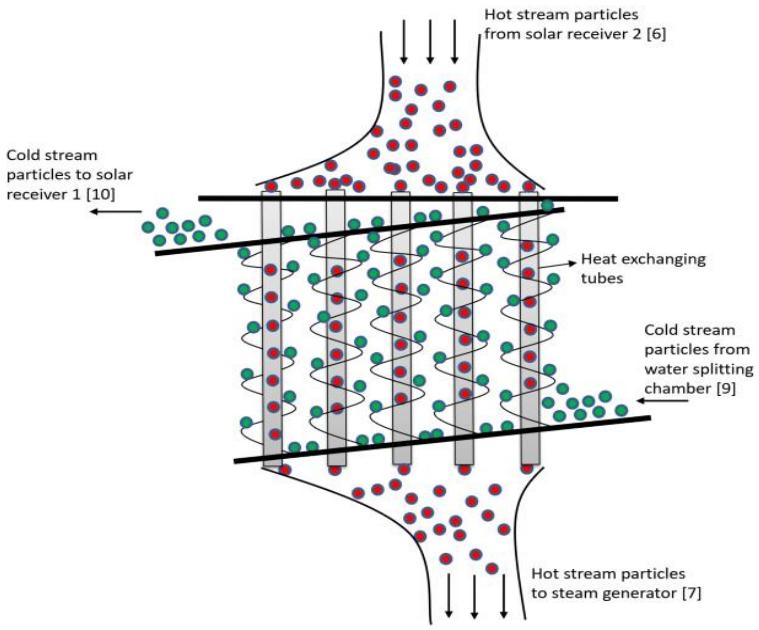

Figure. 3.2 Schematic of solid-solid recuperator

The flow rate of particles in the recuperator is n_p per second and volume of n_p particles including volume fraction, V_n, is given in Eq. 3.4.

$$V_n = \left(\frac{n_p \cdot M_p}{\rho_p}\right) \cdot \left(\frac{1}{F_{vol,rec}}\right) \tag{3.4}$$

where ρ_p is mass density of particles, M_p is molecular weight of the particles and $F_{vol,rec}$ is volume fraction of particles inside the tubes. This is related to the required volume of each tube, $V_{t,rec}$, to equate the volume ratio, R_{vol}, in Eq. 3.5 that is further used to setup a system of four equations in Eqs. 3.6-3.9 for sizing the recuperator in which $d_{t,rec}$ is

diameter of the tube, $h_{t,rec}$ is height of the tube, $\dot{n}_{p,t}$ is flow rate in each tube and t_{rec} is residence time of particles in each tube. Four unknowns, height of each tube, flow rate from each tube, number of tubes and residence time can be solved for by assuming a tube diameter that is kept small maintain sufficient heat transfer from center of the tube to the wall. From Eqs. 3.7 and 3.9 The residence time and number of tubes are always same if the volume ratio is unity. Sensitivity analysis is used to explore the effect of various tube heights.

$$R_{vol} = \frac{V_{t,rec}}{V_n} \tag{3.5}$$

$$\Pi \cdot d_{t,rec} \cdot h_{t,rec} \cdot n_{rec} = A_{rec} \tag{3.6}$$

$$\dot{n}_{p,t} \cdot n_{rec} = \dot{n}_p \tag{3.7}$$

$$\frac{\Pi}{4} \cdot d_{t,rec}^2 \cdot h_{t,rec} = V_{t,rec} \cdot R_{vol} \tag{3.8}$$

$$t_{rec} \cdot \dot{n}_{p,t} = n_p \tag{3.9}$$

3.3.2 Steam Generator

The size of the steam generator is calculated based on the total heat lost by the particles exiting the recuperator- particles are cooled to desired re-oxidation temperature in steam generator. The total heat lost by the particles is supplied to water entering at room temperature and exiting as super-heated steam at desired re-oxidation temperature. The thermodynamic equations for total heat lost by particles and heat gained by water are given in Table 1.1.

A schematic of the steam generator is shown in Fig. 3.3 with particles in free fall around the tubes in which water flows, a design that is analogous to cross flow heat exchanger. Radiation heat transfer is dominant mode of heat transfer and convective heat transfer is negligible between particles and tube outside surface. Once through boiler is considered for this model because the exit temperature of the particles is above 1000 K and there are chances of water boiling at any stage in the steam generator.

The modes of heat transfer between particles-tube outside wall, through the wall, and tube inside wall to fluid are radiation, conduction, and convection respectively. Radiation heat transfer between particles and the outside wall of the tube in the economizer is given by Eq. 3.10

$$\frac{\sigma \cdot A_{p,t} \cdot (T_{p,ec}^4 - T_{o,t,ec}^4)}{R_{sg}} = \dot{Q}_{t,ec} \tag{3.10}$$

$$A_{p,t} = \frac{A_p}{n_t} \tag{3.11}$$

$$\dot{Q}_{ec,t} = \frac{\dot{Q}_{ec}}{n_t} \tag{3.12}$$

where $A_{p,t}$ is total surface area of particles in each tube, $T_{p,ec}$ is average temperature of particles in economizer, $T_{t,o,ec}$ is average outside temperature of tube wall in economizer, R_{sg} is combined surface and geometric radiation resistance, $\dot{Q}_{t,ec}$ is heat transfer per tube in economizer, A_p is total surface area of the particles in all tubes, n_t is number of tubes and $\dot{Q}_{ec}$ is total heat transfer in economizer. Tube diameter and the number of tubes are explored through sensitivity analysis to examine their effect on total area and pressure losses in the steam generator. Calculation of geometric resistance between the particles and

tubes is beyond the scope of this work and this article proposes the maximum value of radiation resistance for this design which is 15.

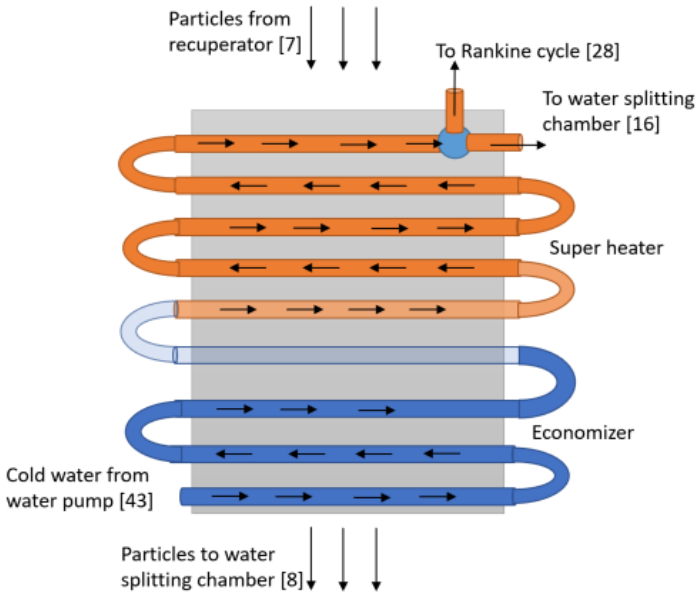

Figure. 3.3 Schematic of steam generator

The conduction heat transfer rate through the tube wall is given in Eq. 3.13

$$\frac{2\cdot л\cdot k_t\cdot L_{t,ec}\cdot(T_{t,o,ec}-T_{t,i,ec})}{Ln(\frac{R_o}{R_i})} = \dot{Q}_{t,ec} \tag{3.13}$$

where k_t is thermal conductivity of tube material, $L_{t,ec}$ is length of each tube in economizer, $T_{t,i,ec}$ is inside wall temperature of tube and R_o and R_i are outer and inner radius of the tube. The convection heat transfer rate between the tube inside wall and water flowing inside the tubes is given by Eq. 3.14

$$л \cdot d_{t,sg} \cdot L_{t,ec} \cdot h_{w,sg} \cdot \left(T_{t,i,ec} - T_{w,sg}\right) = \dot{Q}_{t,ec} \quad (3.14)$$

where $d_{t,sg}$ is diameter of the tube, $h_{w,sg}$ is convection heat transfer coefficient between inside tube wall and water and $T_{w,sg}$ is average temperature of water in economizer. The convection heat transfer coefficient for Eq. 3.14 is calculated using the Eqs. 3.15, 3.16 and 3.17

$$h_{ec} = \frac{Nu_{ec} \cdot K_w}{d_{t,sg}} \quad (3.15)$$

$$Nu_{ec} = \frac{f_{ec} \cdot (Re_{ec} - 1000) \cdot Pr_w}{1 + 12.7 \cdot (\frac{f_{ec}}{2})^{0.5} \cdot (Pr_w^{2/3} - 1)} \quad (3.16)$$

$$f_{ec} = (1.58 \cdot Ln\,(Re_{ec}) - 3.28)^{-2} \quad (3.17)$$

where Nu_{ec} is Nusselt number, k_w is thermal conductivity of water, Re_{ec} is Reynolds number of water inside economizer tubes and Pr_w is Prandtl number. All properties are calculated at the average water temperature in the economizer for the first iteration with the solution repeated until values converges to less than 1% difference between successive iterations. Three unknowns including the length of the tube and the outside and inside temperature of the tube wall are solved for in Eqs. 3.10, 3.13 and 3.14 by assuming a tube diameter, tube thickness and number of tubes that are explored further during sensitivity analysis. These results are used to calculate the bulk mean temperature properties of water and the convection heat transfer coefficient used in the second iterative computation.

The total surface area, A_{ec}, of the economizer is calculated using Eq. 3.18.

$$A_{ec} = л \cdot d_{t,sg} \cdot L_{t,ec} \cdot n_t \quad (3.18)$$

The constraint equations for evaporator are Eqs. 3.19, 3.20 and 3.21.

$$\frac{\sigma \cdot A_{p,t} \cdot (T_{p,ev}^4 - T_{t,o,ev}^4)}{R_{sg}} = \dot{Q}_{t,ev} \tag{3.19}$$

$$\frac{2 \cdot \pi \cdot K_t \cdot L_{t,ev} \cdot (T_{t,o,ev} - T_{t,i,ev})}{Ln(\frac{R_o}{R_i})} = \dot{Q}_{t,ev} \tag{3.20}$$

$$T_{t,i,ev} - T_s = \left(\frac{8 \cdot F_{TS} \cdot \dot{Q}_{t,ev} \cdot T_s}{\Pi \cdot d_{t,sg} \cdot L_{t,ev} \cdot K_l \cdot Q_{lat,w} \cdot \rho_s}\right)^{1/2} \tag{3.21}$$

where $T_{p,ev}$ is average temperature of particles in the evaporator, $T_{t,o,ev}$ and $T_{t,i,ev}$ are evaporator tube outside and inside wall temperatures, $L_{t,ev}$ is length of each tube in evaporator, T_s is saturation temperature of water at corresponding pressure, F_{TS} is surface tension, k_l is thermal conductivity of water at saturation temperature, $Q_{lat,w}$ is latent heat of vaporization at saturation temperature, ρ_s is density of steam at saturation temperature and $\dot{Q}_{t,ev}$ is heat transfer rate per tube in evaporator. Equations 3.19, 3.20 and 3.21 are solved for three unknowns including the length of the evaporator tube and the outside and inside temperature of the tube wall with iterations repeated until convergence. Total surface area of the evaporator is calculated using the Eqs. 3.22.

$$A_{ev} = \pi \cdot d_{t,sg} \cdot L_{ev} \cdot n_t \tag{3.22}$$

The constraint equations for super heater are Eqs. 3.23, 3.24 and 3.25.

$$\frac{\sigma \cdot A_{p,t} \cdot (T_{p,sh}^4 - T_{t,osh}^4)}{R_{sg}} = \dot{Q}_{t,sh} \tag{3.23}$$

$$\frac{2 \cdot \pi \cdot k \cdot L_{t,sh} \cdot (T_{t,o,sh} - T_{t,o,sh})}{Ln(\frac{R_o}{R_i})} = \dot{Q}_{t,sh} \tag{3.24}$$

$$\Pi \cdot d_{t,sg} \cdot L_{t,sh} \cdot h_{s,sg} \cdot \left(T_{t,i,sh} - T_{s,sg}\right) = \dot{Q}_{t,sh} \tag{3.25}$$

where $T_{p,sh}$ is average temperature of particles in the superheater, $T_{t,o,sh}$ and $T_{t,i,sh}$ are super heater tube outside and inside wall temperatures, $L_{t,sh}$ is length of each tube in super heater, $h_{s,sg}$ is convection heat transfer coefficient between inside tube wall and steam and $T_{s,sg}$ is average temperature of steam in super heater. Equations 3.23, 3.24 and 3.25 solve for three unknowns including the length of evaporator tube and the outside and inside temperature of the tube wall with iterations repeated until convergence.

The total surface area of the super heater is calculated in Eq. 3.26 with the total surface area of the steam generator calculated in Eq. 3.27.

$$A_{sh} = \pi \cdot d_{t,sg} \cdot L_{sh,t} \cdot n_t \tag{3.26}$$

$$A_{sg} = A_{ec} + A_{ev} + A_{sh} \tag{3.27}$$

Pressure losses in economizer, evaporator and super heater are calculated using Eqs. 3.28 to 3.33.

$$\Delta P_{ec} = \left(\frac{fr_{ec} \cdot L_{ec} \cdot n_t \cdot \rho_w \cdot V_w^2}{2 \cdot d_{t,ec}}\right) \cdot M_{p,loss} \tag{3.28}$$

$$fr_{ec} = 0.079 \cdot Re_w^{-0.25} \tag{3.29}$$

$$\Delta P_{ev} = \left(\frac{fr_{ev} \cdot L_{ev} \cdot n_t \cdot \rho_{avg} \cdot V_{avg}^2}{2 \cdot d_{t,ev}}\right) \cdot M_{p,loss} \tag{3.30}$$

$$fr_{ev} = -2 \cdot Log\left[\frac{1}{3.7065} \cdot \frac{\varepsilon_{ev}}{d_{t,ev}} - \frac{5.0452}{Re_{mix}} \cdot Log\left(\frac{1}{2.8257} \cdot \left(\frac{\varepsilon_{ev}}{d_{t,ev}}\right)^{1.1098} + \frac{5.8506}{Re_{mix}^{0.8981}}\right)\right] \tag{3.31}$$

$$\Delta P_{sh} = \left(\frac{fr_{sh} \cdot L_{sh} \cdot n_t \cdot \rho_s \cdot V_s^2}{2 \cdot d_{t,sh}}\right) \cdot M_{p,loss} \tag{3.32}$$

$$fr_{sh} = 0.046 \cdot Re_s^{-0.2} \tag{3.33}$$

where $M_{p,loss}$ is pressure loss multiplier accounting to pipe bends, valves and headers, Re_w, Re_{mix}, Re_{sh} are Reynolds numbers for the economizer, evaporator and super heater, respectively, and ε_{ev} is pipe roughness. Total pressure loss in the steam generator is then equated by Eq. 3.34.

$$\Delta P_{sg} = \Delta P_{ec} + \Delta P_{ev} + \Delta P_{sh} \tag{3.34}$$

3.3.3 Hydrogen Separator

The mixture of hydrogen and steam cools in the hydrogen separator with water condensing while hydrogen remains in gaseous form. Heat is recovered from hydrogen sensible heat with additional heat from steam sensible heat, latent heat and water sensible heat. The required heat exchanging area of the hydrogen separator is calculated assuming hydrogen and steam rejects heat separately and the total surface area is the sum of these two parts. Isopentane is selected as the working fluid in the Rankine cycle because of its thermophysical properties. Isopentane is suitable organic fluid for temperatures below 600 K. The molar flow rate of Isopentane is calculated using Eqs. 3.35 and 3.36

$$\dot{n}_{R,st} \cdot \left(\left(c_{p,v,R} \cdot \left(T_{ex,R} - T_{sat,R}\right)\right) + Q_{lat,R} + \left(c_{p,l,R} \cdot \left(T_{sat,R} - T_{in,R}\right)\right)\right) = \dot{Q}_{st} \tag{3.35}$$

$$\dot{n}_{R,h} \cdot \left(\left(c_{p,v,R} \cdot \left(T_{ex,R} - T_{sat,R}\right)\right) + Q_{lat,R} + \left(c_{p,l,R} \cdot \left(T_{sat,R} - T_{in,R}\right)\right)\right) = \dot{Q}_{hy} \tag{3.36}$$

where $\dot{n}_{R,st}$ is the flow rate of steam, $\dot{n}_{R,h}$ is the flow rate of hydrogen, $\dot{Q}_{st}$ is the total heat rejected by steam, $\dot{Q}_{hy}$ is the total heat rejected from hydrogen, $c_{p,v,R}$ is the average specific heat of Isopentane in vapor state, $c_{p,l,R}$ is the average specific heat of Isopentane in liquid state, $T_{ex,R}$ is exit temperature of organic fluid from hydrogen separator in super-heated

state, $T_{in,R}$ is inlet temperature of organic fluid in liquid state, $T_{sat,R}$ is saturation temperature at corresponding pressure and $Q_{lat,R}$ is latent heat of vaporization of organic fluid at saturation temperature.

Based on the inlet conditions and thermodynamic properties of steam and Isopentane the following heat transfer cases occur between the two fluids:

a) Steam cooling and Isopentane vapor is super heating.
b) Steam condensing and Isopentane vapor is super heating.
c) Steam condensing and Isopentane evaporating.
d) Steam condensing and Isopentane liquid is heating.
e) Water cooling and Isopentane liquid is heating.

The total area of the hydrogen separator is sum of areas required based on steam and hydrogen cooling. The area of hydrogen separator based on steam cooling depends on various phases that steam goes through and area is calculated separately for each phase. Individual areas are calculated and summed up to get the total area required.

The required heat transfer area for steam cooling and Isopentane super heating is calculated using Eqs. 3.37, 3.38 and 3.39.

$$\dot{Q}_{st,sh} = \dot{n}_{st,sh} \cdot c_{p,st} \cdot (T_{i,st} - T_{sat}) \tag{3.37}$$

$$\dot{Q}_{st,sh} = \dot{n}_{R,st} \cdot c_{p,v,R} \cdot (T_{ex,R} - T_{sh1,R}) \tag{3.38}$$

$$\dot{Q}_{st,sh} = U_{g-g} \cdot A_1 \cdot LMTD_1 \tag{3.39}$$

where $\dot{Q}_{st,sh}$, $\dot{n}_{st,sh}$ $c_{p,st}$ are total heat rejected by steam, molar flow rate of super-heated steam and average specific heat of super-heated steam, respectively, $T_{i,st}$ is inlet

temperature of super-heated steam and T_{sat} is saturation temperature at corresponding pressure, $T_{sh1,R}$ is temperature of Isopentane vapor when steam starts condensing, U_{g-g} is overall heat transfer coefficient for gas-to-gas and A_1 is area of the super heater when steam is cooling.

The required heat transfer area for steam condensing and Isopentane super heating is calculated using the Eqs. 3.40, 3.41 and 3.42. The flow rate of steam, $\dot{n}_{st}$, is the total steam generated from the hydrogen production subsystem.

$$\dot{Q}_{cond1} = h_{c1} \cdot A_2 \cdot (T_{sat} - T_{sh1,avg}) \tag{3.40}$$

$$T_{sh1,avg} = \frac{T_{sat,R} + T_{sh1,R}}{2} \tag{3.41}$$

$$h_{c1} = 0.729 \cdot \left(\frac{g \cdot \rho_w \cdot (\rho_w - \rho_s) \cdot Q_{lat,hs} \cdot K_w^2}{\mu_w \cdot (T_{sat} - T_{sh1,avg}) \cdot d_{t,hs}}\right)^{1/4} \tag{3.42}$$

where $\dot{Q}_{cond1}$, h_{c1} and A_2 are latent heat drop by steam, convection heat transfer coefficient and super heater surface area when steam is condensing and Isopentane is super heating, respectively, g is acceleration due to gravity, ρ_w and ρ_s are densities of saturated water and saturated vapor, respectively, $Q_{lat,hs}$ is latent heat of vaporization at corresponding pressure, k_w is thermal conductivity of water, μ_w is dynamic viscosity of water and $d_{t,hs}$ is diameter of the tube. The total surface area for the super heater is given by Eq. 3.43.

$$A_{sh,st} = A_1 + A_2 \tag{3.43}$$

The required heat transfer area for steam condensing and Isopentane evaporating is calculated using Eqs. 3.44 and 3.45

$$\dot{Q}_{cond2} = h_{c2} \cdot A_{ev,st} \cdot (T_{sat} - T_{sat,R}) \tag{3.44}$$

$$h_{c2} = 0.729 \cdot \left(\frac{g \cdot \rho_w \cdot (\rho_w - \rho_s) \cdot Q_{lat,hs} \cdot K_w^2}{\mu_w \cdot (T_{sat} - T_{sat,R}) \cdot d_{t,hs}}\right)^{1/4} \quad (3.45)$$

where $\dot{Q}_{cond2}$, h_{c2} and $A_{ev,st}$ are latent heat decrease in steam, convection heat transfer coefficient and evaporator surface area when steam is condensing and Isopentane is evaporating, respectively.

The required heat transfer area for steam condensing and Isopentane liquid heating is calculated using Eqs. 3.46, 3.47 and 3.48

$$\dot{Q}_{cond3} = h_{c3} \cdot A_3 \cdot (T_{sat} - T_{ec1,avg}) \quad (3.46)$$

$$T_{ec1,avg} = \frac{T_{sat,R} + T_{ec1,R}}{2} \quad (3.47)$$

$$h_{c3} = 0.729 \cdot \left(\frac{g \cdot \rho_w \cdot (\rho_w - \rho_s) \cdot Q_{lat,hs} \cdot K_w^2}{\mu_w \cdot (T_{sat} - T_{ec1,avg}) \cdot d_{t,hs}}\right)^{1/4} \quad (3.48)$$

where $\dot{Q}_{cond3}$, h_{c3} and A_3 are latent heat decrease in steam, convection heat transfer coefficient and economizer surface area when steam is condensing and Isopentane liquid is heating, respectively, with $T_{ec1,R}$ as the temperature of Isopentane liquid when steam is fully condensed.

The required heat transfer area for water cooling and Isopentane liquid heating is calculated using Eqs. 3.49, 3.50 and 3.51

$$\dot{Q}_w = \dot{n}_{st} \cdot c_{p,w} \cdot (T_{sat} - T_{ex,w}) \quad (3.49)$$

$$\dot{Q}_w = \dot{n}_{R,st} \cdot c_{p,l,R} \cdot (T_{ec1,R} - T_{in,R}) \quad (3.50)$$

$$\dot{Q}_w = U_{l-l} \cdot A_4 \cdot LLMTD_2 \quad (3.51)$$

where $\dot{Q}_w$, $\dot{n}_{st}$ $c_{p,w}$ are the total heat rejected by water, molar flow rate of total steam entering hydrogen separator and average specific heat of water, respectively, with $T_{ex,w}$ the exit temperature of water, $T_{in,R}$ is inlet temperature of Isopentane, U_{l-l} is overall heat transfer coefficient for liquid-to-liquid and A_4 area of the economizer when water is cooling. The total surface area of the economizer is given by Eq. 3.52.

$$A_{ec,st} = A_3 + A_4 \tag{3.52}$$

These separate area terms are summed to equate the total surface area of the hydrogen separator attributed to steam rejection calculated in Eq. 3.53

$$A_{hs,st} = A_{sh,st} + A_{ev,st} + A_{ec,st} \tag{3.53}$$

The required heat transfer area of the super heater, $A_{sh,hyd}$, based on heat rejected by hydrogen is calculated using Eqs. 3.54, 3.55 and 3.56.

$$\dot{Q}_{sh,hyd} = \dot{n}_h \cdot c_{p1,hyd} \cdot (T_{in,hyd} - T_{hyd,sh}) \tag{3.54}$$

$$\dot{Q}_{sh,hyd} = \dot{n}_{R,st} \cdot c_{p,v,R} \cdot (T_{ex,R} - T_{sat,R}) \tag{3.55}$$

$$\dot{Q}_{sh,hyd} = U_{g-g} \cdot A_{sh,hyd} \cdot LMTD_3 \tag{3.56}$$

where $\dot{Q}_{sh,hyd}$ is heat transfer in the super heater based on hydrogen flow, $\dot{n}_h$ is hydrogen molar flow rate, $c_{p1,hyd}$ is average specific heat of hydrogen in super heater, $T_{in,hyd}$ is temperature of the hydrogen entering hydrogen separator and $T_{hyd,sh}$ is temperature of hydrogen at the end of super heater.

The required heat transfer area of the evaporator, $A_{ev,hyd}$, based on the heat rejected by hydrogen is calculated using Eqs. 3.57 and 3.58

$$\dot{Q}_{ev,hyd} = \dot{n}_h \cdot c_{p2,hyd} \cdot (T_{hyd,sh} - T_{hyd,ev}) \quad (3.57)$$

$$T_{hyd,ev,avg} - T_{sat,R} = \left(\frac{8 \cdot F_{ST,R} \cdot T_{sat,R} \cdot \dot{Q}_{ev,hyd}}{A_{ev,hyd} \cdot K_R \cdot \rho_R \cdot Q_{lat,R}}\right)^{1/2} \quad (3.58)$$

where $\dot{Q}_{ev,hyd}$ is heat transfer in evaporator based on hydrogen flow, $c_{p2,hyd}$ is average specific heat of hydrogen in evaporator, $T_{hyd,ev}$ is temperature of hydrogen at the end of evaporator, $T_{hyd,ev,avg}$ is average temperature of hydrogen in evaporator, $F_{ST,R}$ is surface tension of Isopentane, k_R is thermal conductivity of Isopentane liquid, ρ_R is density of Isopentane vapor and $Q_{lat,R}$ is latent heat of vaporization of Isopentane.

The required heat transfer area of the economizer, $A_{ec,hyd}$, based on hydrogen flow is calculated using Eqs. 3.59, 3.60 and 3.61

$$\dot{Q}_{ec,hyd} = \dot{n}_h \cdot c_{p3,hyd} \cdot (T_{hyd,ev} - T_{ex,hyd}) \quad (3.59)$$

$$\dot{Q}_{ec,hyd} = \dot{n}_{R,st} \cdot c_{p,l,R} \cdot (T_{sat,R} - T_{in,R}) \quad (3.60)$$

$$\dot{Q}_{ec,hyd} = U_{g-l} \cdot A_{ec,hyd} \cdot LMTD_4 \quad (3.61)$$

where $\dot{Q}_{ec,hyd}$ is heat transfer in economizer based on hydrogen flow, $T_{ex,hyd}$ is temperature of hydrogen exiting and U_{g-l} is overall heat transfer coefficient for gas-to-liquid.

These separate area terms are summed to equate the total heat transfer area, $A_{hs,hyd}$, based on hydrogen flow as given in Eq. 3.62. Thereafter, the total heat transfer area, A_{hs}, of the hydrogen separator for mixed steam and hydrogen flow is equated in Eq. 3.63.

$$A_{hs,hyd} = A_{sh,hyd} + A_{ev,hyd} + A_{ec,hyd} \quad (3.62)$$

$$A_{hs} = A_{hs,st} + A_{hs,hyd} \tag{3.63}$$

3.3.4 Water-splitting Reactor

A schematic of water-splitting reactor is shown in Fig. 3.4 illustrating steam flowing upwards and reduced particles flowing downwards in counterflow for an efficient re-oxidation reaction. The velocity of free-falling particles increases as they move downward and thus relative velocity with respect to steam increases. There is no enough time for the re-oxidation reaction if the relative velocity between the particles and steam is high which leads to lower effectiveness of the re-oxidation reaction. The proposed water-splitting reactor design contains multiple vertical and inclined channels to control the velocity of the particles and thus relative velocity between particles and steam. The slope of the inclined surface is chosen such that no particle can go straight down without falling on the inclined surface. Re-oxidation reaction is not expected in the inclined channels as the particles and steam do not contact because of density difference. The total volume, V_{wsr}, of the water-splitting reactor splits into three vertical channels. Height of the inclined channel, $h_{i,wsr}$, is calculated using Eq. 3.66 and diameter is the same as the vertical channel.

$$V_{wsr} = \left(\frac{n_p \cdot M_w}{\rho_p}\right) \cdot \left(\frac{1}{F_{vol,wsr}}\right) \tag{3.64}$$

$$A_{wsr} = \frac{4 \cdot V_{wsr}}{d_{wsr}} + A_{i,wsr} \tag{3.65}$$

$$h_{i,wsr} = \frac{d_{wsr}}{\cos\theta} \tag{3.66}$$

Here $F_{vol,wsr}$ is the volume fraction of particles required in the water-splitting reactor, $A_{i,wsr}$ is sum of surface areas of all inclined channels, A_{wsr} is total surface area, d_{wsr} is diameter of the water-splitting reactor and θ is angle of the inclined channel.

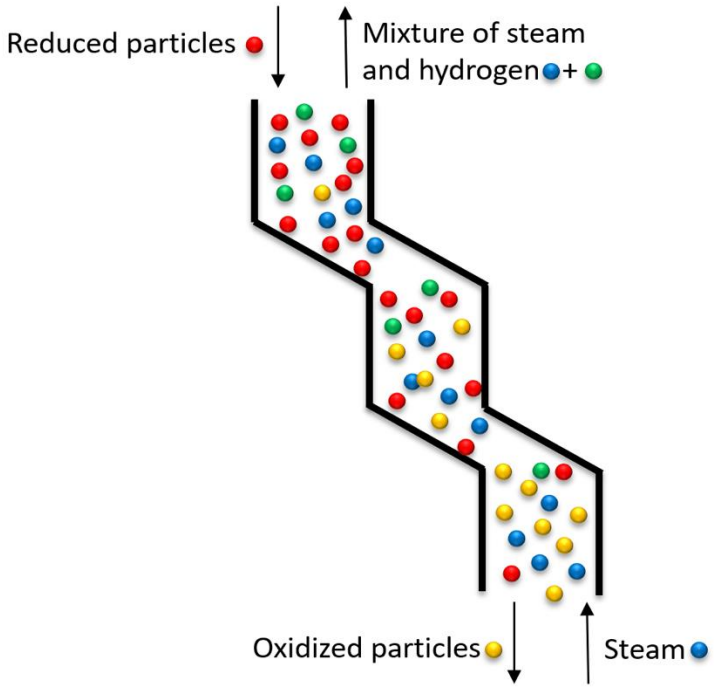

Figure. 3.4 Schematic of water-splitting reactor

3.4. Financial Modeling

The calculated component sizes are used to compute the component capital cost and operating cost for the plant with a 25-year lifetime. Component sizes, scaling functions, complexity multipliers and cost multipliers are used in the various cost functions summarized in Table 3.3. Setting multiplier, P_s, is used to compute installation cost, electrical multiplier, M_e, is used to compute cost of electrical cables and components. Piping multiplier, M_p, is used to compute cost of piping and valves. Receiver multiplier,

M_{rec}, and water-splitting reactor multiplier accounts to complexities involved in fabrication and installation of these components.

Table 3.3. Component cost equations

Component	Cost Equations
Mirrors	$C_{mir} = A_{mir} \cdot C_{mir,sc} \cdot (1 + P_s + M_e)$
Solar field	$C_{sf} = C_{mir} + C_{land} + C_{land,prep}$
Tower	$C_{tow} = H_{tow}^{SF} \cdot C_{tow,sc} \cdot (1 + P_s + M_e)$
Elevator	$C_{ele} = H_{ele}^{SF} \cdot C_{ele,sc} \cdot (1 + P_s + M_e)$
Receivers	$C_{rec} = C_{rec,sc} \cdot A_{rec} \cdot M_{rec} \cdot (1 + P_s)$
Recuperator	$C_{rec} = (HX_O + A_{rec} \cdot HX_1) \cdot (M_{sh}) \cdot (1 + P_s + M_e)$
Steam generator super heater	$C_{sg,sh} = (HX_O + A_{sg,sh} \cdot HX_1) \cdot (M_{sh}) \cdot (1 + P_s + M_e)$
Evaporator and economizer of steam generator	$C_{sg,e} = (HX_O + (A_{sg,ev} + A_{sg,ec}) \cdot HX_1) \cdot (1 + P_s + M_e)$
Hydrogen separator super heater	$C_{hs,sh} = (HX_O + A_{hs,sh} \cdot HX_1) \cdot (M_{sh}) \cdot (1 + P_s + M_e)$
Hydrogen separator evaporator and economizer	$C_{hs,e} = (HX_O + (A_{hs,ev} + A_{hs,ec}) \cdot HX_1) \cdot (1 + P_s + M_e)$
Heat exchangers	$C_{HX} = (HX_O + (A_{HX1} + A_{HX2}) \cdot HX_1) \cdot (1 + P_s + M_e)$
Particles	$C_{par} = m_p \cdot C_{par,sc}$
Water-splitting reactor	$C_{wsr} = A_{wsr} \cdot C_{rec,sc} \cdot M_{rc} \cdot (1 + P_s + C_s)$
Vacuum pumps	$C_{vp} = ((\dot{W}_{30} + \dot{W}_{31}) \cdot m_{vp} + I_{vp} \cdot 4) \cdot (1 + P_s + M_e + M_p)$
Hydrogen pump	$C_{hp} = (\dot{W}_{35} \cdot m_{hp} + I_{hp}) \cdot (1 + P_s + M_e + M_p)$
Steam pump	$C_{sp} = (\dot{W}_{32} \cdot m_{sp} + I_{sp}) \cdot (1 + P_s + M_e + M_p)$
Water pump	$C_{wp} = (\dot{W}_{33} \cdot m_{wp} + I_{wp}) \cdot (1 + P_s + M_e + M_p)$
Rankine cycle	$C_{Ran} = \dot{W}_w^{exp} \cdot C_{Ran,sc}$

The sum of all costs in Table 3.3 gives the total components cost (C_{comp}) per tower. The controls cost (C_{ctr}) and balance of plant cost (C_{BoP}) is calculated using controls factor (f_{ctr}) and BoP factor (f_{BoP}) respectively

$$C_{ctr} = f_{ctr} \cdot C_{comp} \tag{3.67}$$

$$C_{BoP} = (C_{comp} + C_{ctr}) \cdot f_{BoP} \quad (3.68)$$

Contingency cost accounts to uncertainties involved in material and fabrication cost and the total capital expenditure (C_{CapEX}) is calculated using contingency factor (C_{cont})

$$C_{CapEX} = (C_{comp} + C_{ctr} + C_{BoP}) \cdot (1 + C_{cont}) \quad (3.69)$$

Maintenance cost per tower per year is calculated using maintenance factor (f_{main}).

$$C_{main} = (C_{comp} + C_{ctr} + C_{BoP}) \cdot f_{main} \quad (3.70)$$

The capital expenditure per tower per year is estimated from weighted average capital cost factor (f_{wacc}).

$$C_{CapEX,A} = C_{CapEx} \cdot f_{wacc} \quad (3.71)$$

The total plant cost per tower per year is calculated as given in Eq. 72

$$C_{p,tow} = C_{CapEX,A} + C_{main} \quad (3.72)$$

3.5. Input parameters

The input parameters for the sizing and costing calculations are listed in Table 3.4. The total heat transfer rate is the primary input for sizing of recuperator, steam generator and hydrogen separator. The size of the receivers is computed using the ratio of aperture area to total surface area and sensitivity of this ratio is discussed in section 3.6.3.

3.5.1 Equipment sizing

The recuperator is designed for total heat transfer of 26 MW at 0.7 effectiveness. The heat transfer rate from the center of tube to the wall, along the radius, should meet the heat transfer rate between hot and cold particles ($\dot{q}_{rec,t}$) in each tube. The mode of heat transfer along the radius of the tube is through conduction which depends on depends on conductivity of particles and contact resistance and radiation which depends on depends on volume fraction, emissivity and view factor. Calculation this heat transfer rate is beyond the scope this work because of the complexities involved the analysis but it is known fact that heat transfer rate increases with decrease in radius of the tube. The radius of the tube is taken as 25 mm for the preliminary design and sensitivity analysis is discussed in section 3.6.3. The radiation resistance between hot and cold stream particles depends on emissivity of particles and tube wall. The emissivity is assumed as unity for the preliminary design and sensitivity analysis is performed on emissivity of particles.

The steam generator is designed to cool the particles to 1250 K and to produce super-heated steam at 1125 K. The regular steel pipes can be used only below 1000 K because of metallurgical limitations. Since the particles temperature is much above 1000 K throughout steam generator metal alloys with very high melting point need to be considered for steam generator tubes. Nickel or Titanium alloys are most suitable at these temperatures and steel-Nickel alloy is considered in our design. The diameter of the tubes and number of tubes affect total pressure losses affect the size and pressure losses in the component. The sensitivity of inlet water pressure, diameter of the tubes and number of tubes is discussed in section 3.6.3. The other parameter that strongly affects the size of the steam generator is radiation resistance between particles falling downward and tubes. The

geometric radiation resistance depends on position and orientation of particles with respect to tubes and volume fraction since the view of particles obstructs internally. The surface resistance depends on emissivity of particles and tube surface. The calculation of total radiation resistance is beyond the scope this work and considered the maximum allowable radiation resistance with respect to other parameters. The maximum radiation resistance is fixed such that the temperature of tube inside wall is always more than the fluid temperature.

Table 3.4. Input parameters to calculate component sizes

Component	Parameter	Value	Comment
Constants	Stefan-Boltzman constant	$5.68X10^{-8}$ W/m^2-K^4	
	Ambient temperature	298 K	
	Ambient Pressure	1.01325 bar	
Tower	Tower height	90 m	
Receiver	Area ratio	24	Based on the apparatuses geometric configurations being worked at Sandia National Laboratories
Recuperator	Total heat transfer ($\dot{Q}_{rec}$)	26 MW	From Table 1.1
	Particle flow rate ($\dot{n}_p$)	856 mol/s	From Table 1.1
	Diameter of each tube ($d_{t,rec}$)	0.05 m	Engineering assumption
	Radiation resistance (R_{rec})	1	Engineering choice
	Volume ratio (R_{vol})	1	Engineering choice
	Volume fraction ($f_{vol,rec}$)	0.64	Engineering choice
Steam generator	Total heat transfer	10.52 MW	From Table 1.1
	Inlet water pressure	15 bar	Engineering choice
	Tube thermal conductivity ($k_{t,e}$)	25 W/m-K	Material property
	Super heater tube thermal conductivity ($k_{t,sh}$)	20 W/m-K	Material property
	Tube diameter ($d_{t,sg}$)	0.05	Engineering choice
	Number of tubes in economizer and evaporator ($n_{t,e}$)	50	Engineering choice
	Number of tubes in super heater ($n_{t,sh}$)	100	Engineering choice
	Radiation resistance (R_{sg})	15	Engineering assumption
	Pressure loss multiplier ($M_{p,loss}$)	4	Engineering assumption
Water-splitting reactor	Volume fraction ($F_{vol,wsr}$)	10 %	Engineering choice
	Number of vertical and inclined channels	3 and 2	Engineering choice
	Reactor diameter (d_{wsr})	0.42 m	Engineering choice

	Angle of inclined channel	45^0	Engineering choice
Elevator	Elevator height	55 m	[56]
Heat exchangers	Overall heat transfer coefficient (U_{g-g})	40 W/m^2-K	
Hydrogen separator	Total heat rejected by steam ($\dot{Q}_{st}$)	17.54 MW	From Table 1.1
	Total heat rejected by hydrogen ($\dot{Q}_{hy}$)	0.477 MW	From Table 1.1
	Super-heated steam flow rate	120 mol/s	From Table 1.1
	Total steam flow rate	300 mol/s	From Table 1.1
	Hydrogen flow rate	23.35 mol/s	From Table 1.1
	Inlet pressure of Isopentane	7 bar	Engineering choice based
	Degree of superheat of Isopentane	100 K	Organic fluid properties
	Tube diameter	0.05	Engineering choice
	Overall heat transfer coefficient (U_{g-g})	40 W/m^2-K	
	Overall heat transfer coefficient (U_{g-l})	500 W/m^2-K	

Input parameters for the cost estimation are given in Table 3.5. Receiver multiplier and reactor complexity multiplier are used to account for uncertainties and complexities involved in the design of these components. Sensitivity analysis of multipliers, cost of money and maintenance is discussed in section 3.6.3.

Table 3.5. Input values to calculate cost of components

Component	**Parameter**	**Value**	**Comments**
Multiple	Setting percent (P_s)	20%	Estimate values for plant multipliers are obtained from the chemical engineering handbook of process design (Speight 2002)
	Electrical multiplier (M_e)	8.4%	
	Piping multiplier (Mu_p)	6.0%	
Mirrors	Mirror cost per ($C_{mir,sc}$)	170/m^2	[56]
Solar field	Cost of land (C_{land})	\$349,338	[56]
	Cost of land preparation ($C_{land,prep}$)	\$200,00	
Tower	Tower specific cost ($C_{tow,sc}$)	\$26582/m	Based on a fit from existing installed CSP tower costs, where the cost varies with the receiver
	Scaling factor (SF)	0.95	

			rating adjusted to 2015 (Sargent and Lundy 2003
Elevator	Elevator cost ($C_{ele,sc}$)	3928/m	Scaled based on the falling particle SunShot receiver adjusted to 2015 prices
	Scaling factor (SF)	0.95	
Particles	Particle cost (C_{pa})	\$7.5/kg	Based on the actual cost of production of the specific composition of the material (Commodity and Metal Prices n.d.)
	Particle multiplier (M_{pa})	4	Estimate to account for the fabrication of the particles
Receiver	Material cost ($C_{m,r}$)	\$2400/m^2	Based on collaboration and communication with Hany Ansari (Ansari 2017).
	Material factor ($F_{m,r}$)	2.5	Estimate to account for the fabrication of the material
HX	HX Base cost (HX_O)	\$13,832	Both the vacuum pump and heat exchanger costs are scaled based on the process equipment estimation from DOE and adjusted to 2015 costs with CEPCI numbers (US Vacuum n.d.)
	Cost per area (HX_1)	\$185/m^2	
	Super heater material multiplier (M_{sh})	2	
Vacuum Pump	Vacuum pump base cost (Vp_0)	\$4041	
	Vacuum pump scaling cost (Vp_1)	\$1600/kWh	
Water-splitting reactor	Reactor complexity multiplier (M_{rc})		
	Cooling system factor	10%	Engineering assumption
Rankine cycle	Cost per kW	4062	
Balance of Plant	BoP factor	10%	Costs are based on System Advisor Model (SAM) (NREL/TP -5500-57625 2013). Parameters are taken at the same value as SAM, or at a more conservative value to account for any additional uncertainties of the technology.
	Controls factor	5%	
	Weighted average cost of capital ($wacc$)	6% per year	
	Fraction of particle replacement (F_{rep})	10% per year	
	Maintenance	1% per year	

3.6. Results

3.6.1 Component Sizes

The residence time and number of tubes are same as shown in Table 3.6 because the volume ratio is assumed as unity. The heat transfer rate within the tube along the radius should be 0.275 MW otherwise the tube diameter must be decreased which leads to increase in total area of the recuperator. The total height and width of the recuperator depends on the tube height and number of tubes. The width of the recuperator increases as the number of tubes increases and it is difficult to distribute the particles into all tubes equally. The tube height must be within the limitations of tower height which also accommodates receivers, steam generator and water-splitting reactor. The sensitivity of tube diameter, volume ratio and emissivity of particles is discussed in section 3.6.3.

The results of steam generator given in Table 3.6 shows that approximately 85% of the total size of steam generator is super heater because the degree of super heat, difference between exit temperature to saturation temperature of steam, is 654 K. Increasing the water pressure increases the saturation temperature and decreases the degree of super heat which ultimately reduces super heater size. It is extremely important to keep the size of super heater as low as possible because the chances of tube burnt out are more in super heater. The pressure losses accounts to pipe friction and losses bends and headers. The sensitivity of water pressure, tube diameter, number of tubes and radiation resistance is discussed in section 3.6.3.

The results of the hydrogen separator sizing calculations are given in Table 3.6. One third of the condenser size is super heater because of low gag-to-gas overall heat

transfer coefficient. The saturation temperature of steam, at which steams starts condensing, can be increased by increasing the inlet steam pressure. If the inlet steam pressure is more then the condensation starts at higher temperature and gas-to-gas heat transfer reduces thus decreases the size of super heater.

The pressure of the inlet water leaving the pump impacts the size of all heat exchanging components in the system except recuperator. The effect of water pressure on size of steam generator and hydrogen separator is already discussed. Heat exchanger 1 and 2 increase the temperature of water to near saturation point and thus increase in water pressure increases the exit temperature of water from heat exchangers though the heat transfer is same. The water flow rate in heat exchangers is calculated to meet the exit temperature requirement, increase in water pressure leads to decrease in water flow rate in heat exchangers.

Table 3.6. Results of component sizing calculations

Component	Parameter	values
Recuperator	Total surface area (A_{rec})	208.9 m^2
	Volume of each tube ($V_{t,rec}$)	0.02762 m^3
	Height of each tube ($h_{t,rec}$)	14.07 m
	Number of tubes (n_{rec})	94.54
	Residence time (T_{rec})	94.54 Sec
	Particle flow rate from each tube($\dot{n}_{p,t}$)	9.055 mol/s
	Heat transfer rate in each tube ($\dot{q}_{rec,t}$)	0.2750 MW
	Surface area of each tube (a_{rec})	2.2096 m^2
Steam generator	Water saturation temperature	471 K
	Convection heat transfer coefficient in economizer	150 W/m^2-K
	Convection heat transfer coefficient in super heater	70 W/m^2-K
	Area of Economizer and evaporator ($A_{ec} + A_{ev}$)	20.5 m^2
	Area of the super heater (A_{sh})	119.9 m^2
	Total pressure losses in steam generator (ΔP_{sg})	0.8256 bar
Hydrogen separator	Flow rate of Isopentane based on heat rejection by steam ($\dot{n}_{R,st}$)	387.3 mol/s
	Flow rate of Isopentane based on heat rejection by steam ($\dot{n}_{R,hyd}$)	10.5 mol/s
	Saturation temperature of steam	438 K
	Saturation temperature of Isopentane	345.1 K
	Area of the super heater based on steam	369.4 m^2

	Area of the super heater based on hydrogen	6.9 m^2
	Area of economizer and evaporator based on steam	170.5 m^2
	Area of economizer and evaporator based on hydrogen	23.8 m^2
Mirror	Total area	71034 m^2
Receivers	Surface area	117.8 m^2
Water-splitting reactor	Surface area	31 m^2
Heat exchanger 1 and 2	Surface area	80.84 m^2
Vacuum pumps	Total power consumption	0.5174 MW
Steam pump	Power consumption	0.0484 MW
Hydrogen pump	Power consumption	0.249 MW
Water pump	Power consumption	0.012 MW
Preheater	Power consumption	0.61 MW
Rankine cycle	Electricity generation	6.92 MW

3.6.2 Component Costs

Component costs, maintenance costs and financing costs are summarized in Table 3.7 and equate to annual total cost of approximately $2.85M for a single tower producing 515 ton of hydrogen per annum. The solar field is the largest contributor to cost as it includes the cost of mirrors and land. The water-splitting reactor, stages, pumps and tower are other major contributors to total cost. This indicates that the cost of the water spitting reactor and stages can be brought down as the technology of these components evolve. The cost of vacuum pumps can be reduced as pumping efficiency increases and steam pump can be eliminated by increasing the water inlet pressure. The particles cost majorly depends on the residence time of particles in different components. The residence time can be reduced by efficient heating of particles in stages and with improved kinetics in water-splitting reactor. The sensitivity of multipliers, efficiencies and cost parameters on total plant cost is discussed in section 3.6.3.

Table 3.7. Component costs for a single tower

Component	Cost in $	% of total

Solar field	8,337,000	29.45
Stages	3,257,000	11.51
Recuperator	188,923	0.67
Steam generator	160,940	0.57
Water-splitting reactor	4,992,000	17.64
Elevator	227,029	0.80
Tower	2,453,000	8.67
Particles	2,162,000	7.64
Condenser	377,723	1.33
Rankine cycle	909,711	3.21
Pumps	2,447,300	8.65
Heat exchanger 1	68,711	0.24
Heat exchanger 2	83,771	0.30
Water heater	8,000	0.03
Controls	1,283,655	4.54
Balance of plant	1,347,838	4.76
Total	**27,765,466**	**100.00**

The total number of towers to produce 100,000 kg of hydrogen is nearly 71. The revenue from electricity is calculated by estimating the cost of electricity as \$0.04 per kWh. The cost to produce one kg hydrogen based on annual average efficiency of the plant is \$4.40.

Table 3.8. Calculation of cost of one kg of hydrogen production

Variable	Value	Unit
Total capital expenditure (C_{CapEX})	38,097,993	\$
Weighed average capital cost (C_{wacc})	2,285,879	\$
Maintenance cost per year (C_{main})	566,092	\$
Annual capital expenditure ($C_{CapEX,A}$)	2,851,972	\$
Total hydrogen production per tower per year	515,091	Kg
Total electricity generation per tower per year	14,602	MWh
Revenue from electricity	584,092	\$
Net total cost	2,267,880	\$
Cost of hydrogen per kg	**4.40**	**\$**

3.6.3 Sensitivity Analysis

As the diameter of the tube increases height of the tube also increases and number of tubes decreases. The heat transfer rate along the radius within the tube increases as diameter decreases but the tube height is approximately 40 m at 30 mm diameter. Thus, it

is difficult to reduce tube diameter lower than 30 mm without significantly increasing the total height of the tower as shown in Fig. 3.5. The number of tubes also increases as volume ratio decreases as shown in Fig. 3.6. The width the recuperator rapidly increases below 0.7 volume ratio as the number of tubes are approximately 140. This indicates that volume ratio below 0.7 is not suitable for smooth particle flow rate in the recuperator. The tube diameter and volume ratio need to be optimized considering the practical limitations of particle flow and total tower height.

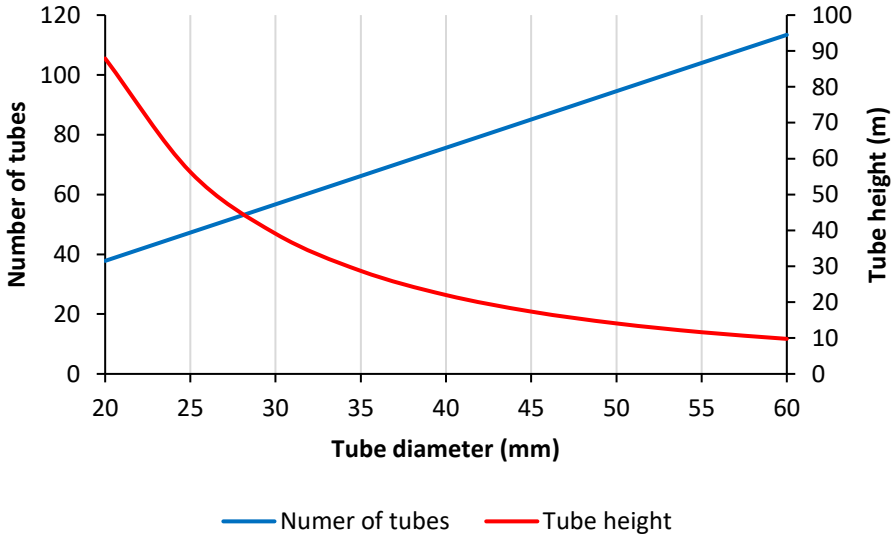

Figure 3.5. Variation of number of tubes and tube height with tube diameter for recuperator at volume ratio unity

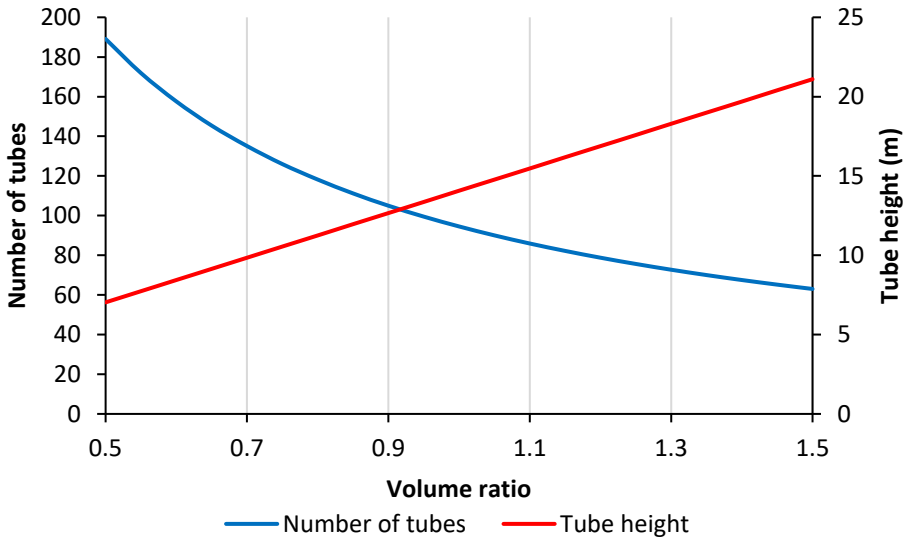

Figure 3.6. Variation of number of tubes and tube height with volume ratio for recuperator at fixed diameter

The water pressure entering the system has a greater impact on the hydrogen separator area than the steam generator area as shown in Fig. 3.7. The total area and super heater area are decreasing at the same rate which indicates that the increase in economizer and evaporator areas are negligible. However, increasing water pressure increases the pumping power and decreases system efficiency indicating that a cost-optimal can be found for this parameter.

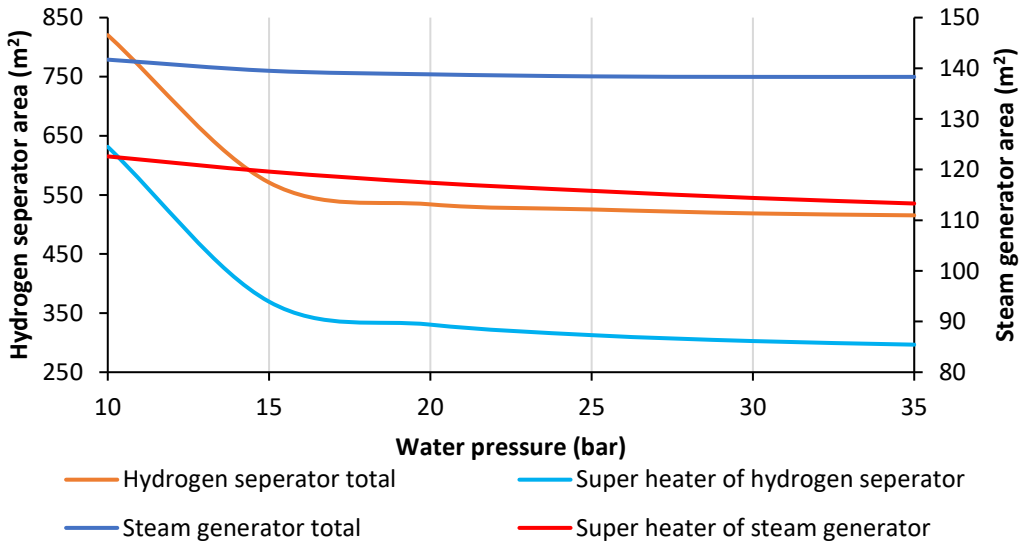

Figure 3.7. Variations of super heater and total size of the components with water pressure

The number of tubes and tube diameter are selected with respect to total pressure losses in the steam generator. The size of steam generator is nearly half at 35 mm diameter compared to 50mm diameter but pressure losses rapidly increases as shown in Fig. 3.8. The total number of tubes and their orientation also affects the radiation resistance which is constrained at a maximum value of 15 in this design. The variation of total steam generator size on radiation resistance is shown in Fig. 3.9.

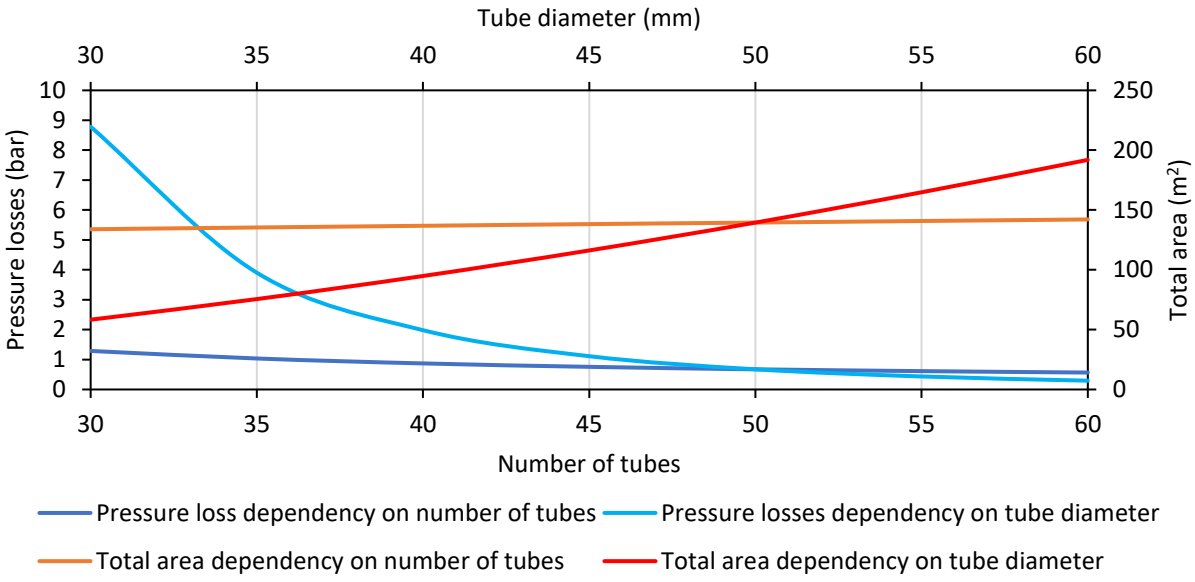

Figure 3.8. Dependency of pressure losses and total area of steam generator on tube diameter and number of tubes

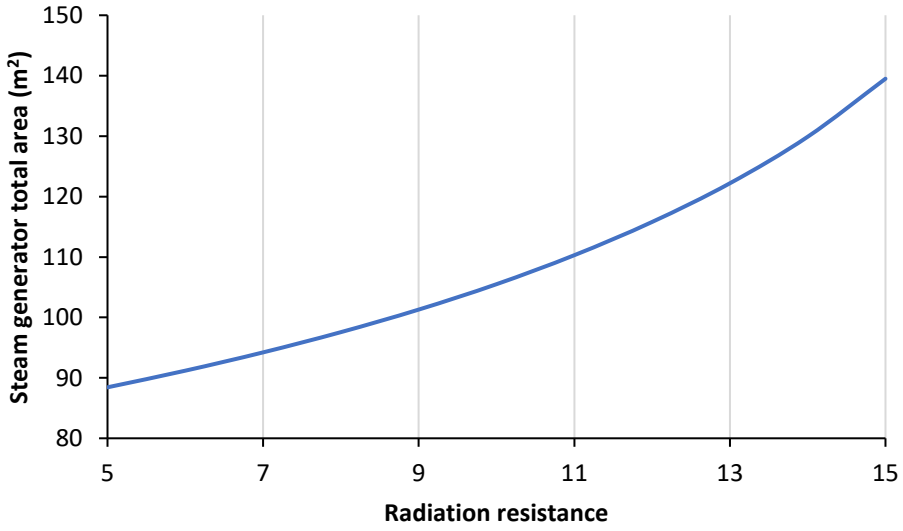

Figure 3.9. Variation of total steam generator area on radiation resistance

Area ratio, stage multiplier, reactor complexity factor, recuperator effectiveness and setting percent have major impact on total plant cost and hydrogen production cost per kg. The decrease in steam generator and hydrogen separator cost at higher water pressures

is offset by an increase in required pumping power. The water pressure can be increased up to 20 bar beyond which pumping cost outweighs the advantage of the decreased cost of other components. The increase in effectiveness of the recuperator increases the hydrogen production but increase in cost of the plant is small. The cost impact of all major variables is listed in Table 3.9.

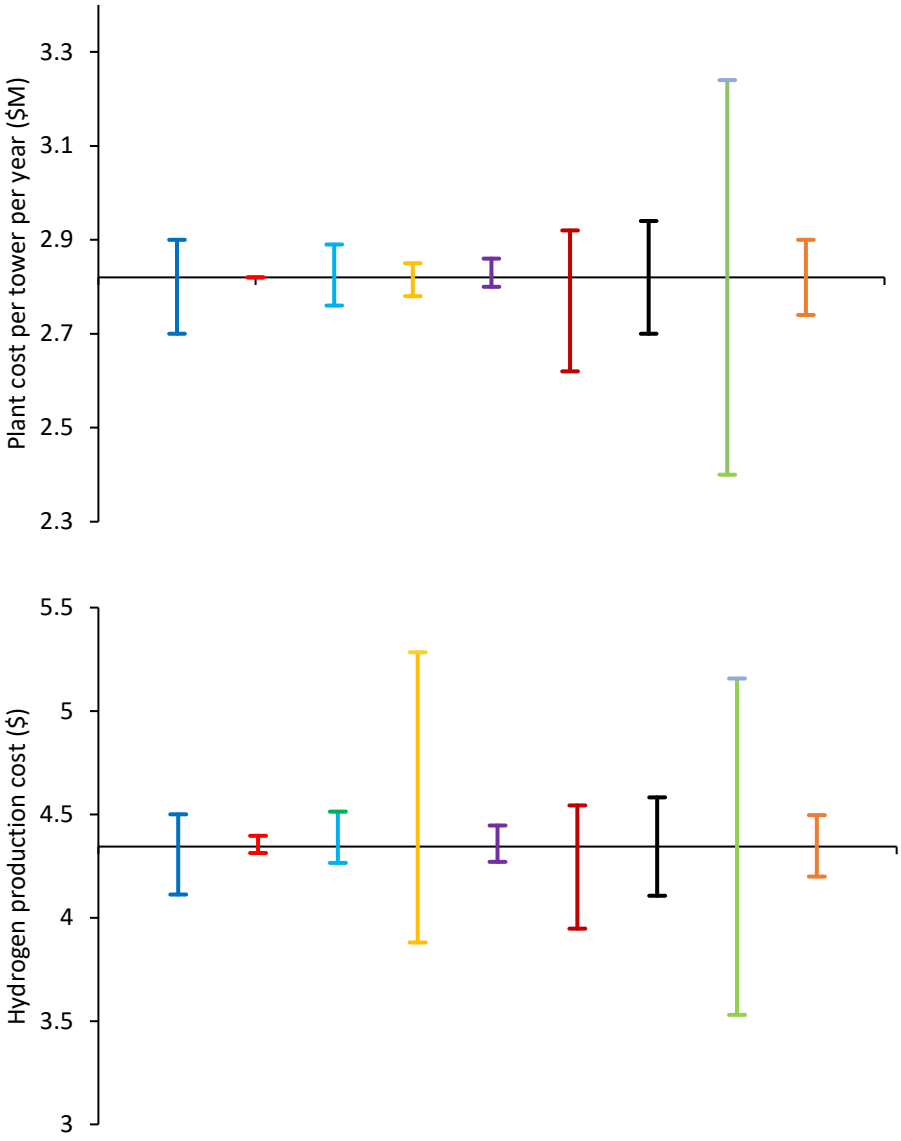

Figure 3.10. Impact of different parameters and cost variables on total cost and hydrogen production cost

Table 3.9. Sensitivity of parameters on cost to produce hydrogen

Symbol	Parameter	Design value	Min / Max	% change in total plant cost	% change in Hydrogen production cost
a	Area ratio	24	15	-3.5	-3.5
			30	+2.3	+2.3
b	Water pressure	15	10	0	0
			30	0	+0.7
c	Stage multiplier	5	4	-1.9	-1.9
			6	+1.9	+1.9
d	Recuperator effectiveness	0.7	0.5	-2.3	+26.1
			0.8	+2.0	-12.1
e	Vacuum pump efficiency (%)	50	40	+1.1	+1.2
			60	-0.7	-0.8
f	Particle multiplier	4	3	-0.8	-0.8
			5	+0.8	+0.8
g	Reactor complexity multiplier	8	6	-4.0	-4.0
			10	+4.0	+4.0
h	wacc (%)	6	5	-0.9	-0.9
			7	+0.9	+0.9
i	Setting percent	20	15	-3.3	-3.3
			25	+3.3	+3.3

The percentage change in component cost and hydrogen production cost by varying design parameters is given in Table 9. Area ratio, stage and reactor complexity multiplier, particle multiplier, wacc, and setting percent impact neither hydrogen production nor system efficiency. Vacuum pump power consumption impacts the system efficiency and increasing the vacuum pump efficiency to 60% decreases the cost of hydrogen by 0.8%. The percentage change in total plant cost with change in water pressure up to 20 bar is negligible but the cost of hydrogen production increases by 0.7% as pumping power increases. The recuperator effectiveness has major impact on the hydrogen and electricity production rate. As the effectiveness increases the hydrogen production rate increases and electricity production decrease and the combined effect of these two production rates on

cost of the plant and cost to produce hydrogen is indicated in the Table 9. If the recuperator effectiveness increases from 0.7 to 0.8 then the increase in plant cost is just 2.0% but the cost to produce hydrogen decreases by 12%.

3.7. Discussion

This study completed system sizing and financial assessment of a concentrating solar power plant with redox active materials to split water and produce 100,000 kg of hydrogen per day on annual average basis with electricity co-production using excess heat to improve financial viability. Component sizes are calculated from the total energy conversion in each component with sensitivity analysis exploring the effect of adjustable design parameters on component sizes, thermodynamic performance, plant cost and the cost of hydrogen. The cost of the hydrogen is calculated from the fixed and running capital, revenue from electricity production and total hydrogen produced in 25 years. The weighted average capital cost per year is $2.85M and cost to produce one kg of hydrogen is $4.40.

This work has proposed a new recuperator design with multiple tubes and calculated the total area of the component based on the design point effectiveness. The recuperator can be designed with different height to width ratios by changing the tube height and number of tubes. The steam generator proposed in this study extracts excess sensible heat in the particles after recupearator. The size of the hydrogen separator was calculated based on the total heat rejected by steam and hydrogen when cooled from water-splitting temperature to room temperature. The size of hydrogen separator is nearly 400% larger than the size of steam generator because of two reasons: (1) the gas-to-gas heat

transfer in hydrogen separator leads to lower heat transfer coefficients and (2) the difference between exit temperature of hot fluid and inlet temperature of cold fluid is very small in hydrogen seperator. The size of the steam generator super heater and hydrogen separator can be decreased by increasing the plant inlet water pressure up to 20 bar, beyond which the required pump size and pumping power begin to add costs that outweigh the financial savings.

Solar field cost is nearly 45% of the total fixed capital and this cost can't be brought down unless the energy requirement of the plant is decreased. Future stage designs will decrease cost and efficient particle heating and water-splitting reactor cost can be reduced with improved reaction kinetics. Recuperator effectiveness has a significant impact on the cost of hydrogen production when noting study findings that an increase in recuperator effectiveness from 0.7 to 0.8 can reduce the cost of hydrogen production by 12% with just a 2% increase in total plant cost. Further cost reductions can be obtained by decreasing the cost of stages, water-splitting reactor and solar field to reach target costs nearer to $2 per kg.

CHAPTER 4

DISCUSSION

Results demonstrate a concentrating solar plant design for a solar thermochemical water splitting process that significantly increases efficiency and reduces cost relatively to other leading studies. An organic Rankine cycle is used to produce electricity from waste heat recovered in the solar to hydrogen production process. System efficiency was calculated to be 39.52% at a design point DNI of 900 W/m^2 with hydrogen fraction and electrical fraction being 50.7% and 49.3%, respectively. The thermodynamic model was evaluated using the redox-active material ceria with the equation sets kept general to permit design parameters and set points to be changed and optimized for other redox active

materials. Two solar receivers were used to reach an oxygen partial pressure of 10 Pa and particle temperature of 1773 K to achieve a reduction extent of 0.031. Additional solar receivers can be added to reach lower oxygen partial pressures for increased particle reduction and cost.

Recuperator effectiveness was found to have a significant effect on hydrogen production and receiver-to-hydrogen efficiency, but only had a minor effect on system efficiency because most of the waste heat was reutilized for electricity production. Total excess heat in the system equates to 21.92 MW, of which 17.73 MW (81%) is recovered from the steam generator, water splitting reactor, hydrogen separator and oxygen stream heat exchangers and transferred to the organic Rankine cycle. The components are sized based on the total energy conversion in each component at design point. Steam generator is designed considering pressure losses, inlet water pressure, and heat transfer coefficients. This work has proposed a new recuperator design with multiple tubes and calculated the total area of the component for 0.7 effectiveness. The recuperator can be designed with different height to width ratios by changing the tube height and number of tubes. This flexibility in design opens number of options to position the recuperator on the tower depending on the size of other components. A steam generator is proposed in this model to extract the excess sensible heat in the particles after recuperator. The mode of heat transfer from the particles is through thermal radiation and thus particles flow pattern plays a significant role in the size of the steam generator. The size of the hydrogen separator is calculated based on the total heat rejected by the steam and hydrogen when cooled from water splitting temperature to room temperature. The size of hydrogen separator nearly 400% larger than the size of steam generator because of two major reasons: (1) The gas-

to-gas heat transfer coefficient in hydrogen separator and the difference between exit temperatures of hot fluid and inlet temperature of cold fluid is very small in hydrogen seperator. Sizes and costs of super heaters can be decreased by increasing inlet water pressure. This cost savings translated to a lower delivered cost of hydrogen up to 20 bar water inlet pressure at which point the increased costs of pumps and pumping power outweighs further cost savings.

The second part of this estimated component sizes and associated costs for a plant designed to produce 100,000 kg of hydrogen per day with electricity co-production using the excess heat in the cycle. The size of each component is calculated based on the total energy conversion in each component with detailed consideration and sensitivity analysis completed on design features and parameters affecting component performance and cost. The cost of hydrogen is calculated from initial capital costs, maintenance costs and financing costs over the 25-year plant life, including revenue from 99.7GWh per year electricity production sold at 0.04 $/kWh. The hydrogen production cost of $4.40 per kg results from annual average cost of $2.85M. The solar field contributes to the largest share of capital cost at 45.8%, with the following leading capital costs including receivers at 7.5%, pumps at 7.1% and water-splitting reactor at 2.2%. The cost of receivers is expected to decrease through ongoing design enhancements on design, with more efficient particle heating and water splitting reactors improving better reaction kinetics and also reducing costs. Improving recuperator effectiveness from 0.7 to 0.8 is a high-value design modification resulting in a 12% decrease in hydrogen cost for a modest 2.0% increase in plant cost. Further cost decreases in the receivers and water splitting reactor with an associated increase in recuperator effectiveness has potential to reduce hydrogen

production costs nearer to $2 per kg. The completed work provides a foundation and generalized set of equations for additional plant designs and techno-economic optimization that seeks to minimize total cost while maximizing revenue from both hydrogen production and electricity.

References

[1] I. Dincer, "Green methods for hydrogen production," *Int. J. Hydrogen Energy*, vol. 37, no. 2, pp. 1954–1971, 2012.

[2] P. E. Dodds *et al.*, "Hydrogen and fuel cell technologies for heating: A review," *Int. J. Hydrogen Energy*, vol. 40, no. 5, pp. 2065–2083, 2015.

[3] N. Sulaiman, M. A. Hannan, A. Mohamed, E. H. Majlan, and W. R. Wan Daud, "A review on energy management system for fuel cell hybrid electric vehicle: Issues and challenges," *Renew. Sustain. Energy Rev.*, vol. 52, pp. 802–814, 2015.

[4] M. Balat and M. Balat, "Political, economic and environmental impacts of

biomass-based hydrogen," *Int. J. Hydrogen Energy*, vol. 34, no. 9, pp. 3589–3603, 2009.

[5] I. K. Kapdan and F. Kargi, "Bio-hydrogen production from waste materials," *Enzyme Microb. Technol.*, vol. 38, no. 5, pp. 569–582, 2006.

[6] M. Balat, "Potential importance of hydrogen as a future solution to environmental and transportation problems," *Int. J. Hydrogen Energy*, vol. 33, no. 15, pp. 4013–4029, 2008.

[7] R. Kothari, D. Buddhi, and R. L. Sawhney, "Comparison of environmental and economic aspects of various hydrogen production methods," *Renew. Sustain. Energy Rev.*, vol. 12, no. 2, pp. 553–563, 2008.

[8] S. Venkata Mohan, Y. Vijaya Bhaskar, and P. N. Sarma, "Biohydrogen production from chemical wastewater treatment in biofilm configured reactor operated in periodic discontinuous batch mode by selectively enriched anaerobic mixed consortia," *Water Res.*, vol. 41, no. 12, pp. 2652–2664, 2007.

[9] I. Ermanoski, N. P. Siegel, and E. B. Stechel, "A New Reactor Concept for Efficient Solar-Thermochemical Fuel Production," *J. Sol. Energy Eng.*, vol. 135, no. 3, p. 31002, 2013.

[10] A. Steinfeld, S. Sanders, and R. Palumbo, "Design Aspects of Solar Thermochemical Engineering—A Case Study: Two-Step Water-Splitting Cycle Using The Fe3O4/FeO Redox System," *Sol. Energy*, vol. 65, no. 1, pp. 43–53, 1999.

[11] R. B. Diver, J. E. Miller, M. D. Allendorf, N. P. Siegel, and R. E. Hogan, "Solar Thermochemical Water-Splitting Ferrite-Cycle Heat Engines," *J. Sol. Energy*

Eng., vol. 130, no. 4, p. 41001, 2008.

[12] C. Agrafiotis, M. Roeb, and C. Sattler, "A review on solar thermal syngas production via redox pair-based water/carbon dioxide splitting thermochemical cycles," *Renew. Sustain. Energy Rev.*, vol. 42, pp. 254–285, 2015.

[13] M. A. Rosen, "Advances in hydrogen production by thermochemical water decomposition: A review," *Energy*, vol. 35, no. 2, pp. 1068–1076, 2010.

[14] A. Steinfeld, "Solar hydrogen production via a two-step water-splitting thermochemical cycle based on Zn/ZnO redox reactions," *Int. J. Hydrogen Energy*, vol. 27, no. 6, pp. 611–619, 2002.

[15] T. Nakamura, "Hydrogen production from water utilizing solar heat at high temperatures," *Sol. Energy*, vol. 19, no. 5, pp. 467–475, 1977.

[16] A. Steinfeld, "Solar thermochemical production of hydrogen - A review," *Sol. Energy*, vol. 78, no. 5, pp. 603–615, 2005.

[17] P. Charvin, A. Stéphane, L. Florent, and F. Gilles, "Analysis of solar chemical processes for hydrogen production from water splitting thermochemical cycles," *Energy Convers. Manag.*, vol. 49, no. 6, pp. 1547–1556, 2008.

[18] J. E. Miller, A. H. McDaniel, and M. D. Allendorf, "Considerations in the design of materials for solar-driven fuel production using metal-oxide thermochemical cycles," *Adv. Energy Mater.*, vol. 4, no. 2, pp. 1–19, 2014.

[19] B. D. Ehrhart, C. L. Muhich, I. Al-Shankiti, and A. W. Weimer, "System efficiency for two-step metal oxide solar thermochemical hydrogen production – Part 1: Thermodynamic model and impact of oxidation kinetics," *Int. J. Hydrogen Energy*, vol. 41, no. 44, pp. 19881–19893, 2016.

[20] I. Ermanoski, “Cascading pressure thermal reduction for efficient solar fuel production,” *Int. J. Hydrogen Energy*, vol. 39, no. 25, pp. 13114–13117, 2014.

[21] S. Brendelberger, M. Roeb, M. Lange, and C. Sattler, “Counter flow sweep gas demand for the ceria redox cycle,” *Sol. Energy*, vol. 122, pp. 1011–1022, 2015.

[22] S. Bilgen, “Structure and environmental impact of global energy consumption,” *Renew. Sustain. Energy Rev.*, vol. 38, pp. 890–902, 2014.

[23] E. De Cian and I. S. Wing, “Global Energy Demand in a Warming Climate,” *Nota di Lav.*, no. 16, 2016.

[24] M. Azhar Khan, M. Zahir Khan, K. Zaman, and L. Naz, “Global estimates of energy consumption and greenhouse gas emissions,” *Renew. Sustain. Energy Rev.*, vol. 29, pp. 336–344, 2014.

[25] P. Nejat, F. Jomehzadeh, M. M. Taheri, M. Gohari, and M. Z. Muhd, “A global review of energy consumption, CO2emissions and policy in the residential sector (with an overview of the top ten CO2emitting countries),” *Renew. Sustain. Energy Rev.*, vol. 43, pp. 843–862, 2015.

[26] G. Walker, “The dynamics of energy demand: Change, rhythm and synchronicity,” *Energy Res. Soc. Sci.*, vol. 1, pp. 49–55, 2014.

[27] M. A. Hannan, F. A. Azidin, and A. Mohamed, “Hybrid electric vehicles and their challenges: A review,” *Renew. Sustain. Energy Rev.*, vol. 29, pp. 135–150, 2014.

[28] S. Jacobsson and A. Johnson, “The diffusion of renewable energy technology: An analytical framework and key issues for research,” *Energy Policy*, vol. 28, no. 9, pp. 625–640, 2000.

[29] D. Popp, I. Hascic, and N. Medhi, “Technology and the diffusion of renewable

energy," *Energy Econ.*, vol. 33, no. 4, pp. 648–662, 2011.

[30] S. O. Negro, F. Alkemade, and M. P. Hekkert, "Why does renewable energy diffuse so slowly? A review of innovation system problems," *Renew. Sustain. Energy Rev.*, vol. 16, no. 6, pp. 3836–3846, 2012.

[31] I. Dincer and C. Acar, "Review and evaluation of hydrogen production methods for better sustainability," *Int. J. Hydrogen Energy*, vol. 40, no. 34, pp. 11094–11111, 2014.

[32] C. C. Agrafiotis, C. Pagkoura, A. Zygogianni, G. Karagiannakis, M. Kostoglou, and A. G. Konstandopoulos, "Hydrogen production via solar-aided water splitting thermochemical cycles: Combustion synthesis and preliminary evaluation of spinel redox-pair materials," *Int. J. Hydrogen Energy*, vol. 37, no. 11, pp. 8964–8980, 2012.

[33] L. Xiao, S. Y. Wu, and Y. R. Li, "Advances in solar hydrogen production via two-step water-splitting thermochemical cycles based on metal redox reactions," *Renew. Energy*, vol. 41, pp. 1–12, 2012.

[34] T. Wiltowski, K. Mondal, A. Campen, D. Dasgupta, and A. Konieczny, "Reaction swing approach for hydrogen production from carbonaceous fuels," *Int. J. Hydrogen Energy*, vol. 33, no. 1, pp. 293–302, 2008.

[35] C. Acar and I. Dincer, "Comparative assessment of hydrogen production methods from renewable and non-renewable sources," *Int. J. Hydrogen Energy*, vol. 39, no. 1, pp. 1–12, 2014.

[36] F. Suleman, I. Dincer, and M. Agelin-Chaab, "Comparative impact assessment study of various hydrogen production methods in terms of emissions," *Int. J.*

Hydrogen Energy, vol. 41, no. 19, pp. 8364–8375, 2016.

[37] E. Cetinkaya, I. Dincer, and G. F. Naterer, "Life cycle assessment of various hydrogen production methods," *Int. J. Hydrogen Energy*, vol. 37, no. 3, pp. 2071–2080, 2012.

[38] S. Z. Baykara, "Hydrogen production by direct solar thermal decomposition of water, possibilities for improvement of process efficiency," *Int. J. Hydrogen Energy*, vol. 29, no. 14, pp. 1451–1458, 2004.

[39] J. D. Holladay, J. Hu, D. L. King, and Y. Wang, "An overview of hydrogen production technologies," *Catal. Today*, vol. 139, no. 4, pp. 244–260, 2009.

[40] J. E. Miller, M. D. Allendorf, R. B. Diver, L. R. Evans, N. P. Siegel, and J. N. Stuecker, "Metal oxide composites and structures for ultra-high temperature solar thermochemical cycles," *J. Mater. Sci.*, vol. 43, no. 14, pp. 4714–4728, 2008.

[41] D. Yadav and R. Banerjee, "A review of solar thermochemical processes," *Renew. Sustain. Energy Rev.*, vol. 54, pp. 497–532, 2016.

[42] W. C. Chueh, M. Abbott, D. Scipio, and S. M. Haile, "High-flux solar-driven thermochemical dissociation of CO 2 and H 2 O using ceria redox reactions," *Science (80-.).*, vol. 63, no. December, p. 2010, 2010.

[43] N. P. Siegel, J. E. Miller, I. Ermanoski, R. B. Diver, and E. B. Stechel, "Factors affecting the efficiency of solar driven metal oxide thermochemical cycles," *Ind. Eng. Chem. Res.*, vol. 52, no. 9, pp. 3276–3286, 2013.

[44] I. Ermanoski, J. E. Miller, and M. D. Allendorf, "Efficiency maximization in solar-thermochemical fuel production: challenging the concept of isothermal water splitting," *Phys. Chem. Chem. Phys.*, vol. 16, no. 18, pp. 8418–8427, 2014.

[45] R. Chacartegui, L. Vigna, J. A. Becerra, and V. Verda, “Analysis of two heat storage integrations for an Organic Rankine Cycle Parabolic trough solar power plant,” *Energy Convers. Manag.*, vol. 125, pp. 353–367, 2016.

[46] Y.-Q. Zhang *et al.*, “Development and experimental study on organic Rankine cycle system with single-screw expander for waste heat recovery from exhaust of diesel engine,” *Energy*, vol. 77, pp. 499–508, 2014.

[47] I. Ermanoski and N. Siegel, “Annual average efficiency of a solar-thermochemical reactor,” *Energy Procedia*, vol. 49, pp. 1932–1939, 2013.

[48] V. Taseska, N. Markovska, and J. M. Callaway, “Evaluation of climate change impacts on energy demand,” *Energy*, vol. 48, no. 1, pp. 88–95, 2012.

[49] M. Helen McCay, “Hydrogen. An Energy Carrier.,” *Futur. Energy Improv. Sustain. Clean Options our Planet*, no. April, pp. 495–510, 2013.

[50] M. Ni, M. K. H. Leung, K. Sumathy, and D. Y. C. Leung, “Potential of renewable hydrogen production for energy supply in Hong Kong,” *Int. J. Hydrogen Energy*, vol. 31, no. 10, pp. 1401–1412, 2006.

[51] M. Ni, D. Y. C. Leung, M. K. H. Leung, and K. Sumathy, “An overview of hydrogen production from biomass,” *Fuel Process. Technol.*, vol. 87, no. 5, pp. 461–472, 2006.

[52] D. Graf, N. Monnerie, M. Roeb, M. Schmitz, and C. Sattler, “Economic comparison of solar hydrogen generation by means of thermochemical cycles and electrolysis,” *Int. J. Hydrogen Energy*, vol. 33, no. 17, pp. 4511–4519, 2008.

[53] J. E. Miller *et al.*, “Development and assessment of solar-thermal-activated fuel production: phase 1 summary,” *Sandia Rep.*, no. July, pp. 1–38, 2012.

[54] S. Abanades and G. Flamant, “Thermochemical hydrogen production from a two-step solar-driven water-splitting cycle based on cerium oxides,” *Sol. Energy*, vol. 80, no. 12, pp. 1611–1623, 2006.

[55] C. P. Falter, A. Sizmann, and R. Pitz-Paal, “Modular reactor model for the solar thermochemical production of syngas incorporating counter-flow solid heat exchange,” *Sol. Energy*, vol. 122, pp. 1296–1308, 2015.

[56] M. Romero, R. Buck, and J. E. Pacheco, “An Update on Solar Central Receiver Systems, Projects, and Technologies,” *J. Sol. Energy Eng.*, vol. 124, no. 2, p. 98, 2002.